Integrating Data-Driven Methods in Nonlinear Dynamical Systems: Control, Sparsity and Machine Learning

Xing Fu

A dissertation
submitted in partial fulfillment of the
requirements for the degree of

Doctor of Philosophy

University of Washington

2014

Reading Committee:

Nathan Kutz, Chair

Emanuel Todorov

Steven Brunton

Program Authorized to Offer Degree:
Applied Mathematics

University of Washington

Abstract

Integrating Data-Driven Methods in Nonlinear Dynamical Systems: Control, Sparsity and Machine Learning

Xing Fu

Chair of the Supervisory Committee:
Professor Nathan Kutz
Department of Applied Mathematics

The goal of my thesis is to provide a theoretical demonstration of how dimension reduction, control and machine learning techniques can be applied to optimize the performance of complex nonlinear systems. Specifically, integrating those methods to build mode-locked fiber lasers that are more robust and with high performances. We show that an adaptive genetic algorithm is successful in increasing pulse energies in a multi-nonlinear polarization rotation(NPR) fiber laser system and in achieving locally optimal performance. In order to maintain the local optimal performance under birefringence perturbations, we designed an extremum seeking controller(ESC). By numerical simulations of a single-NPR fiber laser, it is showed that the ESC tracks local optimal mode-locking states despite significant disturbances to parameters. We also developed a toroidal search and a machine learning algorithm that enables us to obtain a global optimal performance when birefringence of laser cavity varies. In addition, we also demonstrated an adaptive time-stepping method for dimension reduction computation which can be used to accelerate numerical simulations for partial differential equations. Overall, these methods are all data-driven and do not rely upon underlying models and hence can be generalized to use in other non-optical complex systems as well in the future.

TABLE OF CONTENTS

Page

LIST OF FIGURES

ACKNOWLEDGMENTS

First I would like to express sincere appreciation to my advisor, Professor Nathan Kutz. It is his guidance and support that made my work possible, it is his enthusiasm that always inspires me, it is his encouragement that helped me through the worst time. I would like to thank my collaborator Professor Steven Brunton for his help and discussions over these years. I want to thank all my committee members, Professor Nathan Kutz, Professor Emanuel Todorov, Professor Steven Brunton and Professor Martin Afromowitz for their generous help and support. I would also like to thank my colleagues Edwin Ding, Matthew Williams, from whom I learned a lot.

The work in this dissertation is supported by the National Science Foundation (NSF) (DMS-1007621), the U.S. Air Force Office of Scientific Research (AFOSR) (FA9550-09-0174).

DEDICATION

To my wife and parents.

Chapter 1

INTRODUCTION

Originating from statistics and computer science, data-driven methods have revolutionized our world by their impact on engineering and science in the past decade. Use of machine learning and dimensionality reduction techniques allows electronic chips or computers to perform as an expert in the loop to characterize system status, optimize performance and also execute control algorithms under perturbations, therefore significantly improves the usability and reliability of highly complex systems which in old days can only be operated and maintained manually. However, although data-driven methods have been widely applied in the information technology industry and become a necessity in various types of search and recommendation systems, many of these state-of-art technologies have yet to be applied to a wide range of fields. This suggests a huge potential of integrating data-driven methods in those fields. In this thesis, we study how data-driven control, optimization and computation methods can be applied to complex systems. As the showcase, mode-locked lasers are used to demonstrate the improvement in both performance and robustness when data-driven control, optimization and dimension-reduction strategies together with machine learning are integrated to optical systems. Specifically, we studied a genetic algorithm for local optimization, an extremum seeking control for maintaining local optimum under perturbations, and a library building- search technique which utilizes sparsity and enables global optimization of the system. Note that all methodologies above are purely data driven, hence do not rely on underlying governing equations, although at the first place designed for mode-locked lasers, they can be generalized to use in other physical systems without much effort.

The start point is data-driven local optimum search. For complex systems like mode-locked lasers, the dynamics are highly nonlinear and there is no way of representing the dependency of system input and output explicitly as an equality with nice mathematical

properties(differentiability, smoothness etc.), which makes most traditional optimization algorithms lack of power in such case. As a result, an optimization routine that only takes system input and output is much preferred and genetic algorithm fit the needs perfectly. In Chapter 3, an adaptive genetic algorithm is introduced for local optimum searching of a multiple nonlinear polarization rotation(NPR) mode-locked fiber laser which high dimensional parameter space, simulation result shows cavity energy is increased by a factor of five. Another issue that often occurs in complex systems is that the optimum performance can not be maintained under perturbations given that effort has been made to tune the system to achieve optimal status. In Chapter 4, we discuss this issue with a single-NPR mode-locked fiber laser as an example and illustrate how to design objective function and extremum seeking controller for such system. In Chapter 5, a library building and search method for global optimum search is discussed, based on dimension-reduction and sparse-representation, the method enable us to recognize birefringence of the laser fiber and hence accurately locate the parameter values that corresponds to the global optimum performances. In chapter 6 we show how we apply dimension-reduction to scientific computing, an adaptive time-stepping method is introduced, applications of the method to nonlinear partial differential equations(PDE) and error analysis results are also discussed in this chapter.

Chapter 2

MODEL PROBLEMS: MODE-LOCKED LASERS

To demonstrate how data-driven method can be applied generally in complex systems, case studies will be made of mode-locked lasers. In this chapter, we discuss four models that are commonly used to describe mode-locked lasers in mathematical physics, out of which our simulation data is generated.

2.1 Coupled Nonlinear Shrödinger Equation with Jones Matrices

2.1.1 Model of Single-NPR Mode-Locked Laser

The schematic of the single-NPR mode-locked laser is shown in Figure 2.1. We model the laser by describing the intra-cavity pulse evolution in a component by component manner. Thus the nonlinear propagation in the optical fiber is treated separately from the discretely applied waveplates and polarizer each round trip through the cavity. This treatment is discussed in detail in [35].

2.1.2 Coupled Nonlinear Schrödinger Equations

The optical field propagation in the fiber are well-described by the coupled nonlinear Schrödinger equations (CNLS) [26, 47]:

$$\begin{aligned} i\frac{\partial u}{\partial z} + \frac{D}{2}\frac{\partial^2 u}{\partial t^2} - Ku + \left(|u|^2 + A|v|^2\right)u + Bv^2u^* = iRu, \\ i\frac{\partial v}{\partial z} + \frac{D}{2}\frac{\partial^2 v}{\partial t^2} + Kv + \left(A|u|^2 + |v|^2\right)v + Bu^2v^* = iRv. \end{aligned} \tag{2.1}$$

In the above equations, $u(z,t)$ and $v(z,t)$ are the two orthogonally polarized electric field envelopes in an optical fiber. t is time non-dimensionalized by the full-width at half-maximum of the pulse, and z is the propagation distance normalized by the cavity length. The functions u and v are often referred to as the fast and slow components, respectively. K is the birefringence, D is the average group velocity dispersion of the cavity. The nonlinear

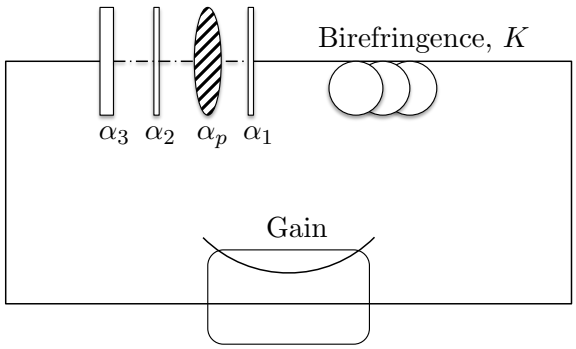

Figure 2.1: Schematic of mode-locked laser with passive nonlinear polarization rotation (NPR). The quarter-waveplate angles are α_1 and α_2, the half-waveplate angle is α_3, and α_p is the angle of the polarizer. There is additionally the birefringence parameter K that arises due to the fiber geometry and its material properties.

coupling parameters A and B correspond to the cross-phase modulation and the four-wave mixing, respectively. They are determined by physical properties of the fiber, and $A+B=1$. For this case (a silica fiber), $A=2/3$ and $B=1/3$. The dissipative terms Ru and Rv account for the saturable, bandwidth-limited gain and attenuation arising from the Yb-doped amplification. The operator R is given by

$$R = \frac{2g_0\left(1+\tau\partial_t^2\right)}{1+(1/e_0)\int_{-\infty}^{\infty}\left(|u|^2+|v|^2\right)dt} - \Gamma,$$

where g_0 is the non dimensional-pumping strength, and e_0 is the non-dimensional saturating energy of the gain medium. The pump bandwidth is τ and Γ quantifies losses due to output coupling and fiber attenuation.

2.1.3 Jones Matrices for Waveplates and Polarizers

The application of the waveplates and passive polarizer after each round trip through the cavity may be modeled by the discrete application of Jones matrices [34, 38, 42]:

$$W_{\lambda/4} = \begin{bmatrix} e^{-i\pi/4} & 0 \\ 0 & e^{i\pi/4} \end{bmatrix}, W_{\lambda/2} = \begin{bmatrix} -i & 0 \\ 0 & i \end{bmatrix}, W_p = \begin{bmatrix} 1 & 0 \\ 0 & 0 \end{bmatrix}.$$

Here, $W_{\lambda/4}$ is the quarter-waveplate (α_1 and α_2), $W_{\lambda/2}$ is the half-waveplate (α_3), and W_p is the polarizer (α_p). If the principle axes of these objects are not aligned with the fast field of the cavity, it is necessary to include the addition of a rotation matrix:

$$J_j = R(\alpha_j)W_j R(-\alpha_j), \quad R(\alpha_j) = \begin{bmatrix} \cos(\alpha_j) & -\sin(\alpha_j) \\ \sin(\alpha_j) & \cos(\alpha_j) \end{bmatrix},$$

where α_j is a waveplate or polarizer angle ($j = 1, 2, 3, p$). These rotation angles will be the control variables, allowing us to find mode-locked solutions. Recent experiments show that these control variables can be easily manipulated through electronic control [23].

2.2 Cubic-quintic Ginzburg-Landau equation

In chapter 6, we will specifically consider this model in the context of mode-locked laser theory [66] so that

$$i\frac{\partial u}{\partial z} + \frac{D}{2}\frac{\partial^2 u}{\partial t^2} + \gamma|u|^2u - \nu|u|^4u = ig(z)\left(1 + \tau\frac{\partial^2}{\partial t^2}\right)u - i\delta u + i\beta|u|^2u - i\mu|u|^4u \tag{2.2}$$

where in the case of mode-locking, gain saturation is provided with the auxiliary equation

$$g(z) = \frac{2g_0}{1 + \frac{1}{e_0}\int_{-\infty}^{\infty}|u|^2dt}\,. \tag{2.3}$$

Here $u(z,t)$ represents the complex envelope of the electric field in the frame of reference of a pulse propagating in a laser cavity. Thus the it is in a boosted reference frame where the independent variables z and t represent distance of propagation and time in the rest fame of the pulse. These optics coordinates essentially treat the z variable as a time-like variable and t as the spatial variable. The dispersion coefficient D characterizes the chromatic dispersion in the laser cavity which is positive for anomalous dispersion and negative for normal dispersion. The cubic and quintic terms, both real and imaginary parts, represent the nonlinear cavity effects arising from the saturating gain-loss in the cavity [12]. The parameters g_0 and e_0 are the saturating gain and energy of the cavity while τ measures the gain bandwidth. Linear cavity losses due to output coupling and attenuation are modeled by the parameter δ.

2.3 Waveguide Arrary Mode-locking

The waveguide array mode-locking (WGAML) model describes the pulse formation and stabilization process in a optical fiber system where saturable absorption if provided by nonlinear, evanescent mode coupling in a waveguide array. Included in the laser cavity is a saturating, bandwidth limited gain which is provided by erbium doped fiber amplification. As with the CQGLE model, the multi-pulsing transition phenomenon is observed. The following equations model the prototypical dynamics of the waveguide array mode-locked laser system [104, 105]:

$$i\frac{\partial A_0}{\partial Z} + \frac{D}{2}\frac{\partial^2 A_0}{\partial T^2} + \beta|A_0|^2 A_0 - ig(Z)(1+\tau\frac{\partial^2}{\partial T^2})A_0 + i\gamma_0 A_0 + CA_1 = 0 \quad (2.4a)$$

$$i\frac{\partial A_1}{\partial Z} + c(A_0 + A_2) + i\gamma_1 A_1 = 0 \quad (2.4b)$$

$$i\frac{\partial A_2}{\partial Z} + cA_1 + i\gamma_2 A_2 = 0 \quad (2.4c)$$

where the saturating gain (L^2 energy control) is given by

$$g(Z) = \frac{2g_0}{1 + \|A_0\|^2/e_0}\,. \quad (2.5)$$

Here A_0, A_1, A_2 are the envelope of the electric field in waveguides 0, 1, 2 respectively. Note that the Z variable is the time-like variable while T is the space-like variable for this system. This is consistent with optics coordinates which are written in the frame-of-reference of the propagating pulse. Saturating gain is only provided to the central waveguide 0. Thus the evolution equation for A_0 is affected by the gainbandwith τ and gain strength/saturation parameter g_0 and e_0. The normalized parameters in the WGAML are as following: D represent the strength and type of chromatic dispersion, β is the strength of the Kerr nonlinearity, τ is the bandwidth of the gain, γ_j is the linear loss in the jth waveguide and C is the strength of coupling between adjacent waveguide.

2.4 Two-dimensional Cubic-quintic Ginzburg-Landau equation

The two-dimensional cubic-quintic Ginzburg-Landau equation is proposed to model cavity soliton formation [107], essentially it is a two-dimensional generalization of the CQGLE already considered. However, the physical role of temporal dispersion is replaced by spatial

diffraction. The 2D-CQGLE describes the time evolution of cavity solitons confined in the transverse spatial dimensions of a transverse laser cavity [107]:

$$i\frac{\partial u}{\partial t} + \frac{D}{2}\nabla^2 u + \gamma|u|^2 u - \nu|u|^4 u = iRu \tag{2.6}$$

where$\nabla^2 = \partial_x^2 + \partial_y^2$ is the two dimensional Laplacian operator in the transverse plane and R is the dissipation operator defined as

$$R = g(t)(1 + \tau\nabla^2) - \delta + \beta|u|^2 - \mu|u|^4 \tag{2.7}$$

with the saturating gain given by

$$g(t) = \frac{2g_0}{1 + \|u\|^2/e_0}\,. \tag{2.8}$$

Here $u(x, y, t)$ represents the averaged complex electric field envelope in the cavity and is dependent on time t and the spatial transverse variables x and y. The parameter D denotes the averaged diffraction coefficient and is positive (negative) for systems with positive (negative) refractive index. The parameters γ and ν are the cubic and quintic self-phase modulation terms respectively that are created by the combined effect of the nonlinear crystal and the saturable quantum well. The gain $g(t)$ depends on the input pump strength g_0 and the total cavity energy given by $\|u\|^2 = \int_{-\infty}^{\infty}\int_{-\infty}^{\infty}|u|^2 dxdy$ which is parametrized by the saturating energy e_0. Additionally, the bandwidth of the gain is limited, only allowing certain spatial frequencies to be amplified. The range of admissible frequencies is controlled by the bandwidth parameter τ. The parameter δ characterizes the total loss of the laser while β describes the intensity discrimination in the laser. The quintic loss term associated with μ saturates the cubic gain term in order to prevent the soliton solution from blowing up.

The soliton solutions supported by the equation are determined by the supplied amplification, which can be controlled by the pumping strength g_0 or the saturating energy e_0. In the numerical experiments, the saturating energy e_0 is fixed. Thus the gain level can be controlled by g_0 completely. More energy is injected to the laser cavity when g_0 is increased resulting in the solution bifurcating from a single-pulse solution to a double-pulse solution, for instance. Further increasing g_0 can generate steady-state three-pulse and four-pulse solutions as well.

Chapter 3

GENETIC ALGORITHMS FOR LOCAL OPTIMIZATION OF COMPLEX SYSTEMS

3.1 Overview

In this chapter[1], we theoretically demonstrate that in a laser cavity mode-locked by nonlinear polarization rotation (NPR) using sets of waveplates and passive polarizer, the energy performance can be significantly increased by incorporating multiple NPR filters. The NPR filters are engineered so as to mitigate the multi-pulsing instability in the laser cavity which is responsible for limiting the single pulse per round trip energy in a myriad of mode-locked cavities. Engineering of the NPR filters for performance is accomplished by implementing a genetic algorithm that is capable of systematically identifying viable and optimal NPR settings in a vast parameter space. Our study shows that five NPR filters can increase the cavity energy by approximately a factor of five, with additional NPRs contributing little or no enhancements beyond this. With the advent and demonstration of electronic controls for waveplates and polarizers, the analysis suggests a general design and engineering principle that can potentially close the order of magnitude energy gap between fiber based mode-locked lasers and their solid state counterparts.

3.2 Introduction

Over the past two decades of its development, mode-locked lasers have continued to make tremendous strides in engineering performance, both in terms of output energy and peak powers. Indeed, Richardson et al. [1] observed that in the past decade alone an average factor of 1.7 per year increase in power has been achieved, yielding approximately a two orders of magnitude power increase in the decade. Moreover, they note that this increase in performance is much more pronounced than increases in their solid-state counterparts.

[1]Content of this chapter is published in journal article [67]

Such performance gains have raised hopes that fiber lasers, whose significant advantageous over solid-state designs are highlighted by Richardson et al. [1], may eventually provide a practical and low-cost engineering solution that competes directly with today's solid state lasers.

To be more directed in our mode-locking appraisal, the focus of this chapter will be on one of the most commercially successful mode-locked lasers developed to date: a nonlinear polarization rotation (NPR) based passive fiber laser cavity that uses a combination of waveplates and a polarizer for achieving saturable absorption [2]. Laser cavities based upon this operating principle have evolved from delivering soliton-like mode-locking with pulse energies of approximately 0.1 nJ to delivering more exotic propagation behavior and mode-locking pulse shapes. In particular, dispersion-managed (stretched-pulse) soliton lasers deliver ≈1 nJ [3–5], similariton lasers peak around 10-20 nJ [6–8], and the ANDi laser design [9] is capable of achieving energies of approximately 40 nJ. Despite the tremendous performance increases, there is a ubiquitous and fundamental power/energy limitation that must be considered: the so-called multi-pulsing instability (MPI) [10–13]. MPI is the critical impediment for the design and optimization of high-performance fiber lasers. Indeed, MPI imposes limitations on both NPR based lasers as well as those whose saturable absorption are generated from quantum dot doped fibers [14], carbon nanotubes [15, 16] and/or graphene [17–19].

Given its impact, methods for circumventing or suppressing MPI are highly desirable. Very recently, it was shown by Li et al. [20], based upon a geometrical viewpoint of the transmission curves [13], that adding one extra set of waveplates and polarizers generates a second nonlinear transmission function which allows for the suppression of the MPI effect. Specifically, it was demonstrated through numerical simulations that the cavity energy could be doubled in the dual-NPR configuration. In this chapter, we develop further the idea of multiple transmission functions for enhancing performance. In particular, we demonstrate that adding multiple sets of waveplates and polarizers allows for significant suppression of the MPI effect, thus allowing for increase in the cavity energy by a factor of 5. For an ANDi laser [9], such an engineering solution would allow one to reach 200 nJ per pulse in energy from the fiber laser. However, engineering such performance is difficult to do

in practice given the tuning required in the angles of the three waveplates and polarizer for generating the desired transmission curve for each NPR. Thus in addition to exploiting multiple transmission curves, we develop an optimization algorithm, based upon a genetic algorithm, that allows for effective exploration and evaluation of the high-dimensional parameter space. This allows for an efficient method for finding regions of peak performance and energy enhancement. Without such an algorithm, using many transmission curves generates an intractable engineering problem.

The chapter is outlined as follows. In Sec. 2, the principle of operation is outlined with emphasis given to a geometrical interpretation of the effective transmission curve [13]. Section 3 introduces the NPR laser cavity equations which are governed by the coupled nonlinear Shrödinger equations (CNLS) with Jones matrices introduced to model the saturable absorption induced by the the NPR. In section4, a multi-grid genetic algorithm is developed in order to solve the parameter tuning problem introduced by the multiple NPRs. The numerical simulation results, which show significant energy enhancement, are shown in Sec. 5. The chapter is concluded in Sec. 6 with a summary of the results and comments about the future outlook of such MPI suppression strategies.

3.3 Principle of Operation

The key ideas for engineering the transmission curve for performance enhancement are developed by Li et al. [13,20]. These ideas will be briefly revisited here in order to motivate the use of multiple transmission curves for significant energy gains in the cavity. To begin, it is well known that the standard combination of waveplates and polarizer in a mode-locked cavity produces a periodic transmission curve. In most theoretical models, most notably the commonly used master equation [2], the transmission curve is Taylor expanded about the first transmission peak, thus resulting in a cubic or cubic-quintic model for the saturable absorption of the waveplates and polarizer. Such theoretical treatments are thus incapable of modeling the multiple transmission peaks necessary for achieving the high energy mode-locking advocated here.

To be more precise, the geometrical description developed previously [13] shows that the multiple transmission windows can be exploited to stabilize and push mode-locked

pulses to higher-energy states. Key to achieving this goal is the ability to engineer the transmission curve, which can be done by adjusting the waveplate and polarizer angles. Indeed, the geometrical description showed that proper engineering of the transmission curve could allow mode-locking to naturally occur on the higher transmission windows instead of going through the MPI. These findings where recently confirmed by full component-by-component simulations of the laser cavity with two sets of waveplates/polarizer [20]. Indeed, by proper engineering, the cavity energy could be doubled with the inclusion of a second set of waveplates and polarizer.

To illustrate the concept in principle, consider the combination of transfer functions, denoted by T_j with $j = 1, 2, ..., N$, which are each produced by a particular setting of the waveplates and polarizer. Figure 3.1 demonstrates the physical setup that captures the fundamental principle expounded. In Fig. 3.1(a), a physically realizable cavity is shown with N sets of waveplates and polarizers. Each of these sets generates a nonlinear, periodic transmission T_1, T_2, ... , T_N respectively. A detail of each section of the fiber laser is shown in Fig. 3.1(b) where the waveplate and polarizer dynamics produces the transmission response T_j. In both Fig. 3.1(a) and (b), the gain elements are optional in the systems. It can be adopted to amplify the pulse after each NPR if desired, giving more flexibility in the engineering design of the transmission function. As shown in Li et al. [20], additional gain elements are not necessary required for achieving higher-energy mode-locking.

As a concrete example, consider the case of two transmission curves (two waveplate and polarizers). The overall cavity transmission curve as a function of the electric field energy E is approximated by the combination

$$T(E) = T_2(T_1(E)E)T_1(E) \tag{3.1}$$

where $T(E)$ is the effective transmission curve generated from the successive application of T_1 and T_2. It is this flexibility that allows for the creation of the ideal transmission curves suggested for overcoming MPI [13]. Essentially, this allows for the generation of transmission functions T_1 and T_2 that have significantly different periodic openings in their transmission windows. Figure 3.2 demonstrates the basic principle by illustrating both a single periodic transmission function, T_n (with $n = 1, 2$) along with the effective transmission

function $T(E)$ given by (3.1). The dotted line is the instability boundary, i.e. the small signal transmission regime, where noise fluctuations will create a new pulse in the cavity. Thus if the transmission window drops below the dotted line, MPI will occur [13, 20]. By concatenating two transmission functions, the effective transmission function can be engineered which allows for significant suppression of the MPI window as a function of input (and output) energy (Fig. 3.2(b)).

Given the demonstrated suppression of MPI by two transmission functions, it is natural to consider the case of N transmission functions for pushing the MPI instability point out even further. The geometrical representation shown in Fig. 3.2 is a bit simplistic, thus requiring a detailed analysis of a realistic laser cavity. And herein lies one of the significant difficulties of such an analysis: how can one explore the vast parameter space required to achieve realistic results. Indeed, each transmission function (See Fig. 3.1(b)) has three waveplate settings $(\alpha_{j,1}, \alpha_{j,2}, \alpha_{j,3})$, a polarizer setting $(\alpha_{j,p})$, birefringence adjustment that can be made through polarization ears and gain settings (two parameters). Thus for any single transmission curve, there are seven parameters that nonlinearly effect the resulting transmission function. Optimizing over a single transmission function is already a difficult task. Optimizing over multiple transmission functions is almost intractable. However, we have developed a genetic algorithm that systematically explores viable solutions and optimizes cavity energy and performance. With the very recent advent of electronically controlled waveplates and polarizers [23], it is not difficult to imagine combining the electronic control with the genetic algorithm to achieve significant improvements in mode-locking performance as well optimal cavity design and control.

3.4 Methematical Model

In order to verify the theoretical predictions of energy enhancement obtained by multiple transmission filters, full simulations of the laser cavity are necessary. The model for describing each fiber section and laser component shown in Fig. 3.1 can be divided into two parts [12,24]: (i) the fiber propagation dynamics which includes the interaction of chromatic dispersion, self-phase modulation, birefringence, cavity attenuation/loss, and bandwidth limited gain and saturation, (ii) the discrete effect of the waveplates and polarizers modeled

by Jones matrices [12, 24]. The effect of the discrete components is to produce an effective saturable absorption effect on the propagation. These components are often lumped into the governing equations and their sinusoidal transmission approximated through a Taylor expansion [12], this produces the Haus master equation [2]. However, the full sinusoidal transmission can be retained if one is interested, as we are, in producing solutions which are stable in the higher transmission window peaks [12].

As discussed in Sec 2.1.2, the normalized intra-cavity dynamics in j-th fiber section is modeled by coupled nonlinear Schrödinger equations (CNLS) [25, 26], while the effect of the waveplates and polarizer is modeled by their corresponding Jones Matrices. The CNLS model together with the Jones matrices provides a full description of pulse propagation and mode-locking dynamics in the laser system shown in Fig 3.1. The full simulation of the multiple filters laser system involves iterations (or round trips in the cavity) of solving the CNLS and then applying the Jones matrices of waveplates and polarizers for each fiber section consecutively in the sequence shown in the experimental configuration. The discrete application of Jones matrices after each cavity round trip acts like a filter that can be tuned to control the mode-locking behavior. Indeed, the waveplate and polarizer settings are critical in engineering the transmission curves $T_n(E)$ for each segment in the laser cavity. The ability to mode-lock pulses is generally closely related to the orientations of the Jones matrices.

3.5 The Genetic Algorithm for Optimizing Laser Performance

The addition of NPRs to the laser cavity has already been demonstrated to improve mode-locking performance [20]. But the results presented by Li et al. [20] were limited to two NPRs since no strategy was developed for optimizing the extremely large parameter space generated by the waveplates and polarizers. The current chapter solves this problem by proposing a genetic algorithm for searching through the high-dimensional, and highly-nonlinear, parameter space. This allows for a constructive, algorithmic search through parameter space to optimize not only the parameter settings, but to ensure that the laser mode-locks.

In the full cavity model (Sec 2.1.2)-(Sec 2.1.3), each additional NPR brings in, at minimum, six additional parameters into the mode-locking dynamics: $\alpha_{j,1}$,$\alpha_{j,2}$,$\alpha_{j,3}$,$\alpha_{j,p}$,$e_{0,j}$ and

$g_{0,j}$. For what follows, we will assume that the birefringence K is constant. This parameter can also be easily brought into the optimization procedure. As a consequence, each new NPR (and existing NPR as well) needs to be tuned so that the model produces mode-locking. By adjusting the value of existing NPR parameters along with the new introduced NPR parameters, the goal is produce a mode-locked state whose optimal output energy exceeds its previous optimal value. Due to the fact that the full cavity model is highly nonlinear, i.e. it is governed by nonlinear partial differential equation with discrete components, there are few optimization strategies capable of addressing the best performance as a function of its NPR parameters. Simply sweeping through parameter space ultimately leads to an intractable problem as each NPR gives six degrees of freedom in a sweep search. Thus brute force methods will fail, especially as the number of NPR components are added to the cavity. One of the few algorithms available capable of optimizing such a system is the genetic algorithm, which belongs to the family of evolutionary algorithms. Although there are no guarantees about its ability to convergence we choose the genetic algorithm because the genetic algorithm is one of the few effective methods for dealing with complicated optimization problems where nonlinear or discontinuous constraints are imposed and traditional method no longer hold.

The genetic algorithm is a searching routine that mirrors the process of natural evolution and genetic mutations. That is, it evolves a population of feasible solutions towards potentially better solutions. In particular, given a set of feasible trial solutions (one pulse per round trip mode-locked states), an objective function (the energy) is evaluated. In the next step, solutions that give the minimum (maximum energy) values of the objective function are kept and mutated (perturbed) in order to potentially achieve a better minimization. This process is repeated through a number of iterations, or generations, with the hope that better and better solutions are generated.

To be more precise about the algorithm, consider the parameter optimization problem for the full cavity model. Since we are looking for the parameters that generate one-pulse mode-locked solutions with the maximum pulse energy, the objective function is constructed as follows

$$minimize\,[-E(\mathbf{x})N(\mathbf{x})] \tag{3.2}$$

where vector $\mathbf{x}$ contains all the parameters of the full cavity model, i.e. the waveplate and polarizer settings, for example, and

$$E(x) = \int_{-\infty}^{\infty} |u|^2 + |v|^2 dt \tag{3.3}$$

, is the mode-locked pulse energy ($E > 0$) with the indicator function

$$N(\mathbf{x}) = \begin{cases} 1 & \text{For stationary single pulse solution} \\ 0 & \text{Else} \end{cases} \tag{3.4}$$

Recall that u and v are solutions to the full cavity model described in Section 3. Different techniques can be applied to recognize whether the solution generated represents a single mode-locked pulse per round trip, thereby determining the value of the indicator function $N(\mathbf{x})$. Thus the indicator function throws out all solutions that are not mode-locked or represent two or more pulses per round trip.

Suppose that m initial guesses are given for vector $\mathbf{x}$ and denote that the the i-th initial guess as $\mathbf{x}_i$ where $i = 1, 2, ..., m$. In next step (generation), m solutions of the full cavity model and the corresponding energies are computed. The simulation of the laser dynamics starts from initial white noise and it is simulated over a sufficiently long time so that mode-locking, if it is in a favorable parameter regime, occurs. The energies of the mode-locked solutions (non mode-locked states are discarded) are compared with each other after each generation and ordered so that the first $p < m$ gives the smallest values of the objective function. Then,

$$\mathbf{x}_i, i = 1, 2, ..., p$$

are kept while

$$\mathbf{x}_i, i = p+1, p+2, ..., m$$

are discarded. As a supplement to the $m - p$ discarded parameter sets, $m - p$ new trial parameter sets ($\mathbf{x}_k$ where $k = m-p, ..., m$ are randomly mutated from the p best objective function values. This process is repeated for a finite number of generations. One can also build a control loop on the algorithm which enables the algorithm to continue runing until the objective function value potentially converges.

Note that in order to implement the genetic algorithm parameter search, we are required to solve for the full cavity evolution (2.1) along with repeated application of N NPR waveplates and polarizers. Thus there are $6\times N$ parameters that are adjusted during the genetic algorithm search. Moreover, the computational cost is significant given that full laser cavity simulations over hundreds of roundtrips is required in order to determine if the solution has mode-locked to a single pulse per round-trip state. Such a method is extremely computationally cumbersome. Thus to save computation time, a multi-grid genetic algorithm is developed, the idea is to first do a genetic algorithm search on a course grid. If it converges, another round of genetic algorithm search in a smaller range based on the previous result is conducted on a finer (more expensive) grid. This helps in efficiently using the genetic algorithm and exploring the parameter space.

In practice, a real laser cavity has many advantages over the computational model developed here. In particular, mode-locking in a real cavity happens on the order of milliseconds or less. Thus, one can imagine implementing the above genetic algorithm where an evaluation of an entire generation could potentially happen in less than a minute using electronic servo controls as suggested in Ref. [23]. This could lead to a cavity self-tuning for optimal mode-locking in a matter of several minutes or tens of minutes. And once tuned, the genetic algorithm could *control* the system by keeping it close to the ideal, optimized energy state. Given the factor of five enhancement in the energy achieved in mode-locking, this is an attractive option which is feasible in practice. It should also be noted that the proposed algorithm could also be modified to find the *dissipative soliton resonance* curve and enforce the precise balance of physical effects leading to an increase mode-locked pulse energy [21, 22]. Thus the genetic algorithm has broader functionality than that advocated and specified here.

3.6 Simulation Results

To demonstrate the results of the genetic algorithm and associated energy enhancement from using multiple transmission filters, simulations of the governing equation (2.1) are performed. The simulations are done using a spectral-based methods where the equation is solved in the Fourier domain for the time (spatial-like variable) and advanced in propagation

Table 3.1: Pulse Energy

1NPR	2NPR	3NPR	4NPR	5NPR	6NPR
2.4976	5.5611	6.5144	9.2303	11.2576	11.3226

distance (time-like variable) using an adaptive 4th-order Runge-Kutta stepper. The primary advantage of the technique is the highly advantageous accuracy properties of the spectral representation.

Simulation results for the laser cavity are performed for 1-, 2-, 3-, 4-, 5- and 6-NPR filters, i.e. the genetic algorithm is used to optimize each of these cavity configurations by prescribing the best settings for the waveplates and polarizers in each of the NPR elements. Figure 3.3 demonstrate the stable mode-locking dynamics for each of these cases. The initial condition in each case is a white-noise (cold cavity) start. Thus the mode-locked states demonstrated can be achieved in practice. It is clear from the dynamics that mode-locking is quickly achieved and that the more NPRs, the higher the peak power and energy in the mode-locked pulse. The demonstrated mode-locked states are just below the MPI threshold and represent the best performance for each cavity considered. Figure 3.4 shows a direct comparison of the mode-locked pulse shapes for the cavity with 1-, 2-, 3-, 4-, 5- and 6-NPR filters. Note that the cavity energy and peak power increases as the number of NPR filters are added. However, it is found through computation that beyond 5 NPR filters, there appears to be little or no increase in the optimal pulse energy and peak power. Thus using 5-NPRs seems to maximize the laser performance at about 5 times the single NPR cavity energy. Table 3.1 gives the (normalized) energy achieved for the mode-locked states shown in Figs. 3.3 and 3.4. In our simulation studies, it was first necessary to find a set of parameters that enabled stable mode locking. This was then used as the starting point for the optimization performed by the genetic algorithm. As an illustration of the optimization routine, Table 3.2 shows the various polarizer settings required for the 5-NPR filter.

Table 3.2: Waveplate and polarizer settings for optimizing 5-NPRs

	$\alpha_{1,j}$	$\alpha_{2,j}$	$\alpha_{3,j}$	$\alpha_{p,j}$	$g_{0,j}$	$e_{0,j}$
j=1	0.0000^0	72.0000^0	38.4740^0	79.2824^0	1.9502	1368.2425
j=2	0.0000^0	72.0000^0	32.3239^0	72.0000	1.8339	1.0000
j=3	0.0000^0	85.3534^0	41.0947^0	72.0000	1.5497	0.6477
j=4	0.0000^0	81.2847^0	38.7435^0	85.8394	1.0000	2.0000
j=5	0.0000^0	90.8970^0	37.4666^0	72.0000	1.9619	0.3786

3.7 Summary

Although the MPI effect is ubiquitous in fiber laser cavities, our theoretical and computational studies suggest that it can be circumvented and suppressed by engineering the transmission function appropriately. As a result, significant pulse energy enhancements are possible. Numerical simulations which include component by component modeling of the fiber laser cavity using the standard coupled nonlinear Schrödinger equation model along with Jones matrices for the waveplates and polarizers shows that the addition of additional NPR filters are capable of significantly enhancing mode-locking performance. In our numerical simulations, a two-fold energy increase is achieved under the 2-NPR configuration, while a factor of 2.6, 3.7 and 4.5 increase is achieved for 3-NPR, 4-NPR and 5-NPR configurations respectively. The addition of NPRs for mitigating MPI and increasing cavity energies is critical in the effort to close the order of magnitude gap in energy performance between fiber lasers and their solid-state counterparts.

To implement the multiple NPR scenario in practice, a new strategy is developed to optimize the cavity performance in the vast parameter space represented by the multiple NPRs. In particular, the key difficulty present in engineering an appropriate transmission function for each NPR concerns the selection of the parameters for the extra NPRs (waveplates, polarizers, gain, etc). As a results, we developed a multigrid genetic algorithm with a built-in pulse recognition routine as the parameter optimization tool. It is a viable and

efficient method for searching the high-dimensional parameter space for physically realizable parameter settings which allow for higher single-pulse energies. Indeed, this algorithm can be adopted and modified as a control algorithm for implementation in a physically realizable fiber laser where electronic control can be established over the various parameters [23]. This control algorithm would enable one to control the pulse energy, peak power, bandwidth etc. in the laser cavity dynamically even under the influence of perturbations (changes in temperature, birefringence, position of polarizers).

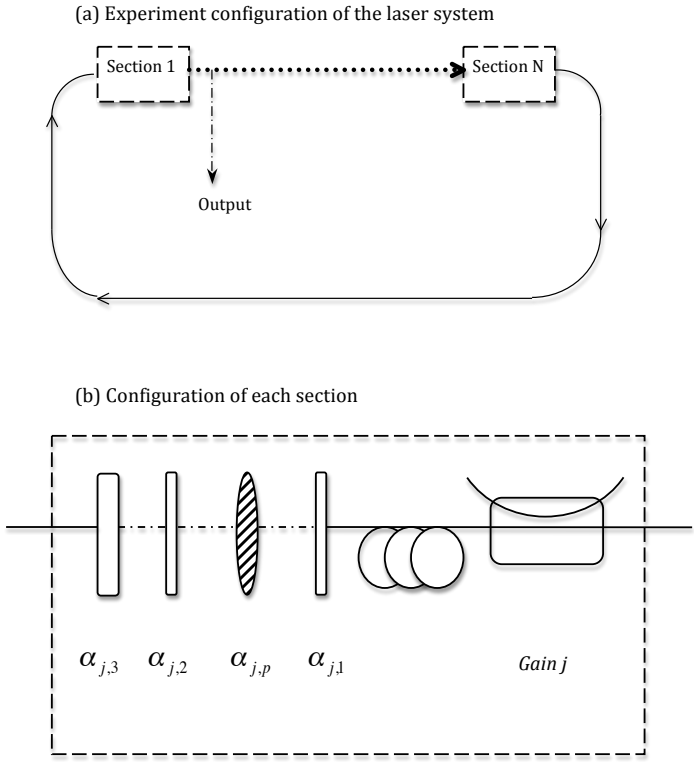

Figure 3.1: (a) Experimental configuration of the multiple transmission filters ring cavity laser system that includes N NPR sections. The output of the lasers is taken between the 1st and 2nd NPR section. (b) Each NPR section contains two quarter-wave plates ($\alpha_{j,1}$ and $\alpha_{j,2}$), one half-wave plate ($\alpha_{j,3}$), one passive polarizer ($\alpha_{j,p}$), one amplifier and one gain source. Thus a minimum of 6 parameters must be tuned in each NPR section.

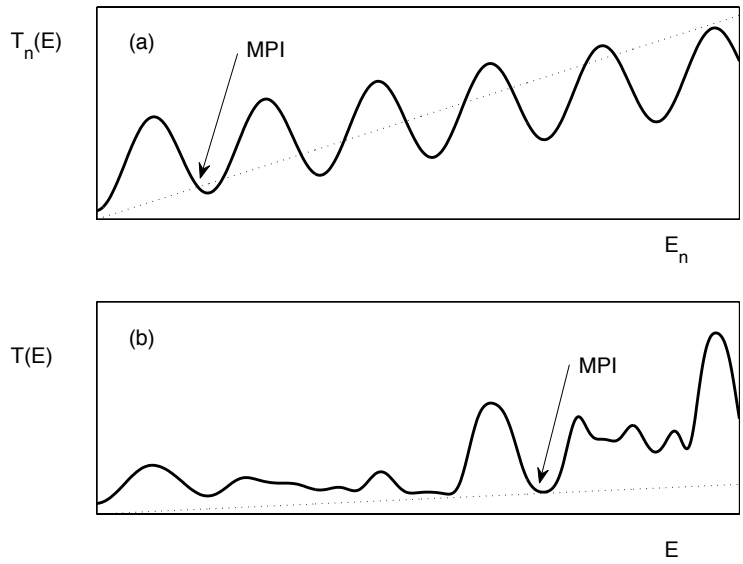

Figure 3.2: (a) Prototypical example of the periodic transmission function $T_n(E)$ of a single NPR. As shown in Ref. [13, 20], the onset of MPI occurs when the transmission curve intersects the small signal gain threshold (dotted line). Thus noise fluctuations below the dotted line would produce a new mode-locked pulse and induce MPI. (b) Prototypical example of the transmission function $T(E)$ given two periodic transmission filters used together as in (3.1). In this case, the onset of MPI is greatly suppressed and higher energy mode-locked states can be achieved [20]. Our goal is to engineer $T(E)$ using multiple transmission curves in order to achieve optimal mode-locking performance.

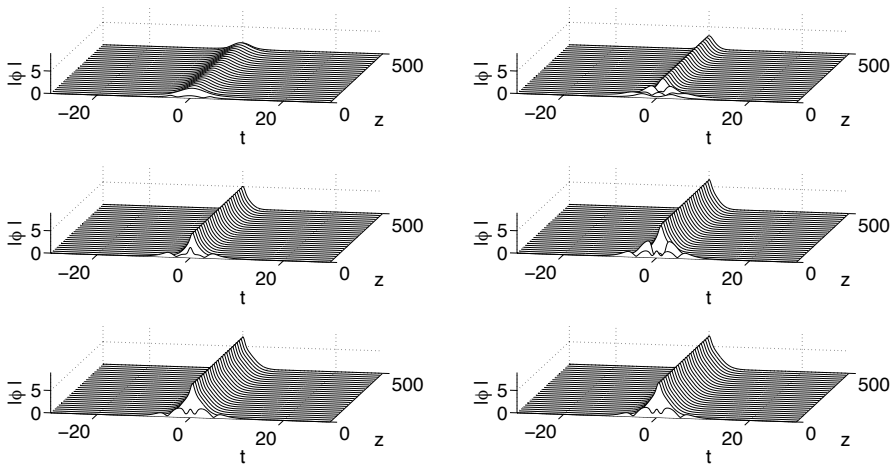

Figure 3.3: Optimal mode-locking dynamics achieved for a laser cavity with 1-, 2-, 3-, 4-, 5- and 6-NPR filters (top left to bottom right). A factor of 5 improvement can be made with the inclusion of additional filters.

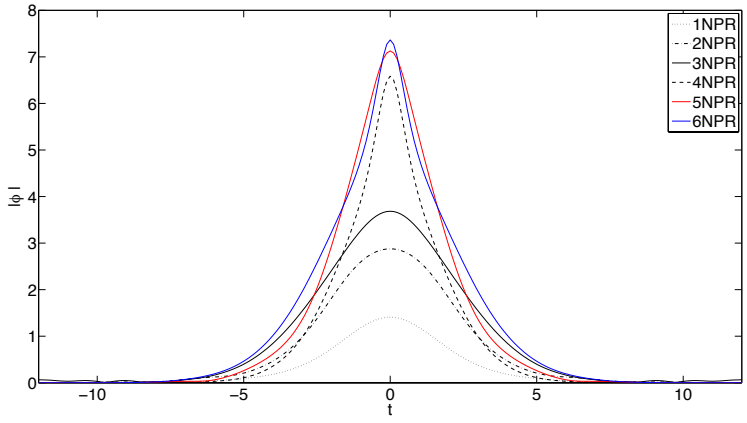

Figure 3.4: Optimal mode-locking states achieved for a laser cavity with 1-, 2-, 3-, 4-, 5- and 6-NPR filters (top left to bottom right). A factor of 5 improvement can be made with the inclusion of additional filters.

Chapter 4

EXTREMUM-SEEKING CONTROL OF COMPLEX SYSTEMS

4.1 Overview

In this chapter[1], we demonstrate that an adaptive controller is capable of both obtaining and maintaining high-energy, single-pulse states in a mode-locked fiber laser. In particular, a multi-parameter extremum-seeking control (ESC) algorithm is used on a nonlinear polarization rotation (NPR) based laser using waveplate and polarizer angles to achieve optimal passive mode-locking despite large disturbances to the system. The physically realizable objective function introduced divides the energy output by the kurtosis of the pulse spectrum, thus balancing the total energy with the coherence of the mode-locked solution. Moreover, its peaks are high-energy mode-locked states that have a safety margin near parameter regimes where mode-locking breaks down or the multi-pulsing instability occurs. The extremum seeking controller is demonstrated by numerical simulations of a single-NPR mode-locked laser and is able to track locally maximal mode-locked states despite significant disturbances to parameters such as the fiber birefringence.

4.2 Introduction

Mode-locked lasers are characterized by the locking of multiple axial modes in the laser cavity, thus resulting in resonant, ultrashort pulsing phenomenon [1, 2, 7, 53, 54, 66]. Over the past decades, such mode-locked lasers have become commercially and scientifically successful, impacting medical imaging [40], two-photon microscopy [33,60], femtosecond chemistry [61], micro-machining [37,45], surgery [39,55–57], and fusion research [36], for instance. Fiber-based mode-locked lasers are particularly interesting due to the numerous inherent advantages of the optical fiber platform [1]. Recent trends have shown that these fiber-based lasers may eventually achieve competitive performance with their solid-state coun-

[1]Content of this chapter is published in journal article [68]

terparts [1, 28], thus potentially shifting the field of ultra-fast, high-power lasers to fiber based technologies. Closing the order of magnitude performance gap between fiber and solid-state lasers will require the ability to control and optimize laser cavity output energy and pulse-width. This motivates the extremum-seeking control advocated here whereby optimal cavity performance can be achieved even with a large parameter space and the effects of considerable perturbations to the cavity.

One of the most prolific and dominant fiber-based mode-locking lasers demonstrated to date involves a linear polarizer and a number of waveplates to achieve saturable absorption via nonlinear polarization rotation (NPR) [2, 35, 49, 104]. Such passive mode-locking is compact, comparatively inexpensive, reliable, and requires less optical tuning compared with alternative ultrafast laser technologies. However, the multi-pulsing instability (MPI) imposes a fundamental performance limit on the mode-locked laser cavity, thus preventing fiber lasers from achieving the desired solid-state performance levels [42]. To overcome MPI, it was recently demonstrated that two (or more) NPR sections (dual transmission filters) could increase the pulse energy output [20] by circumventing MPI at high gains [10–13]. Combined with the recent experimental demonstration of electronic control of waveplates and polarizer [23], a genetic algorithm could be implemented to search through the high-dimensional parameter space for multiple-NPR lasers in order to find high-energy mode-locked solutions [67].

Even with such potential advancements, it remains challenging and expensive to find high-energy, single-pulse solutions in the multiple-NPR case. Moreover, even if mode-locking is achieved, it may be destroyed by changes to the birefringence [26, 47], which often varies throughout the day and may change abruptly if the laser system is physically perturbed [41]. This requires commercial lasers based upon NPR, for instance, to enforce strict environmental control in order to maintain performance, i.e. the fiber is pinned into place and protected from temperature fluctuations.

Alternatively, feedback control promises significant performance enhancements, including maintaining high-energy, mode-locked pulses despite large variations in parameters (e.g., birefringence, thermal/optical, etc.), as suggested in [1]. However, feedback control typically involves a detailed model of the underlying dynamics, and many of the most powerful

tools only apply to linear or nearly-linear systems. In the mode-locked laser, the underlying dynamics are strongly nonlinear, and the variation with respect to parameters is difficult to model. In particular, the fiber birefringence lacks a precise, quantitatively accurate model for its fluctuations and dependence on bending, temperature, etc.

Extremum-seeking control (ESC) is an adaptive method of finding local maxima of an objective function on the output of a dynamical system that bypasses many of the aforementioned issues. The controller does not require a model of the underlying dynamics, which is advantageous for complex, nonlinear systems with parameter dependence that is difficult to model, such as the laser cavity birefringence, which can easily corrupt performance. Extremum-seeking has recently been made mathematically rigorous [27,32,43], and stability guarantees have been proven under certain conditions.

Extremum-seeking control has been applied to a wide range of problems, including maximum-power point tracking for photovoltaic power optimization [30, 31, 44] and wind turbine optimization [48], reducing the noise of a jet [46], active shear layer control for drag reduction in fluids [51], maximizing the pressure rise in an axial flow compressor [59], optimizing bioreactors [58], controlling the current profile in a Tokamak [50], and in active braking systems for automobiles [62]. The above examples involve a single control variable, using what is known as *single-parameter* extremum seeking. Multi-parameter extremum seeking, involving the simultaneous control of multiple inputs, has been applied to the problem of formation flight [29], and also to laser pulse shaping [52].

In this chapter, we apply multi-parameter extremum seeking control to find and maintain locally optimal single-pulse laser solutions. A single-NPR cavity laser is simulated according to the model described in Section 4.3, and a new objective function is developed in Section 4.4 that has high-energy mode-locked pulses as local maxima. The extremum-seeking control architecture is described in Section 4.5. Section 4.6 contains the numerical results demonstrating the effectiveness of the adaptive controller both to find local maxima for fixed birefringence, and to track these high-energy, single-pulse solutions when the birefringence is varying. The variations in birefringence may be viewed as a general disturbance to the system, either due to thermal fluctuations, or physical perturbations to the laser system. The results are summarized in Section 4.7, and future directions are discussed,

Table 4.1: Single-NPR computational parameters

τ	Γ	A	B	D	K	g_0	e_0	L_t	N_t
0.1	0.1	2/3	1/3	-0.4	0.1	1.73	4.23	60	256

including the extension of these methods to multiple-NPR cavities in experiments.

4.3 Model and Numerical Integration Scheme

A schematic of the laser is shown in Figure 2.1. We model the laser by describing the intra-cavity pulse evolution in a component by component manner. Thus, as showed in section 2.1.2, the nonlinear propagation in the optical fiber is treated separately from the discretely applied waveplates and polarizer each round trip through the cavity. This treatment is discussed in detail in [35].

The CNLS equations are solved in the spectral domain by using the fast Fourier transform (FFT) along with an adaptive-step, fourth-order Runge-Kutta scheme to integrate initial conditions one round trip through the cavity. The Jones matrices are then applied to model the discrete application of waveplates and polarizer, and the entire process is repeated. Mode-locking spontaneously arises from white-noise initial conditions after a short number of round trips. The numerics used in this work are an extension of the methods developed in [35, 67]. Typical parameters used in these simulations are given in Table 4.1. The round-trip length is 1.5 dimensionless units.

4.4 Objective Function

For any extremum-seeking controller to be effective, we require an objective function with local maxima that correspond to high-energy mode-locked solutions. Although we seek high-energy solutions, there are many chaotic waveforms that have significantly higher energy than mode-locked solutions. Therefore, energy alone is not a good objective function. Instead, we divide the energy function (E) by the kurtosis (κ) of the Fourier spectrum of the waveform, which is large for undesirable chaotic solutions. This objective function is large when we have a large amount of energy in a tightly confined temporal wave packet.

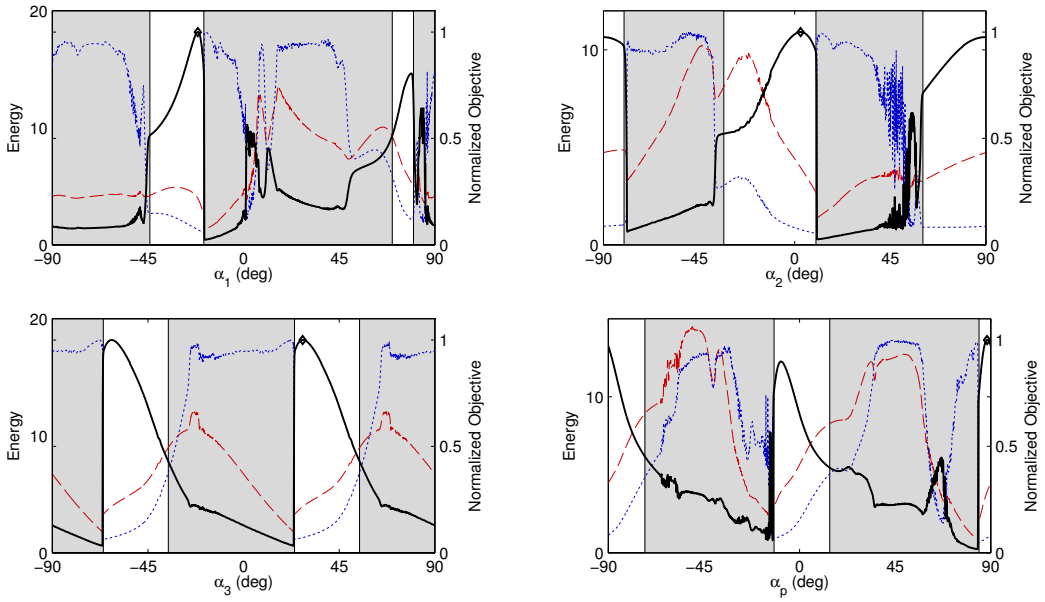

Figure 4.1: Objective function E/κ (solid black), energy E (dashed red) and kurtosis of the spectrum κ (blue dots) for varying waveplate and polarizer rotation angles $\alpha_1, \alpha_2, \alpha_3$ and α_p. Single-pulse mode-locking occurs in the white regions. As each angle is varied, all other angles are held fixed at locally maximizing values, indicated by black diamonds.

The kurtosis of a signal x is given by the fourth moment about the mean divided by the square of the variance: $\kappa = E\left[(x-\bar{x})^4\right]/E\left[(x-\bar{x})^2\right]^2$.

Figure 4.1 shows the new objective function (solid black), energy (red dash), and the kurtosis of the spectrum (blue dots) for various slices of the rotation angles α_j. In each panel, one of the angles is rotated from $-90°$ to $90°$ while the other angles are held fixed at values that locally maximize the objective function. These locally optimal values are obtained by applying the extremum-seeking controller developed in the next sections. In each panel, the maximal energy occurs away from the regions of single-pulse mode locking, shown by the white-regions, and tracking energy alone would lead to chaotic solutions (grey regions). In contrast, the new objective function has local maxima in the single-pulse mode-locked regions, and there is a buffer between the peak in objective function and the grey region where mode-locking fails. The white regions are determined manually by checking if the solution has a single pulse. These regions are not used by the control algorithms, but are included to illustrate the regions of stability. The spectral kurtosis (blue dots) is small in the single-pulse mode-locking regions (white) and is much larger in the grey regions because of multi-pulse or chaotic solutions. Thus, dividing energy by the spectral kurtosis penalizes non-mode-locking solutions.

It may be tempting to use an angle that is right at the edge of the white region with higher energy, for example in the third panel in the second white region. These edge points, although they do contain more energy, correspond to fat mode-locked pulses and are not as favorable as the tight pulses at the peak of the black curves. In addition, being close to the grey boundary makes this solution susceptible to disruption by any manner of disturbance to the system (e.g., birefringence, thermal optical, etc.).

Consider Figure 4.2, which is a zoom-in of the third panel of Figure 4.1. As we vary α_3 with all of the other angles held fixed, the energy function increases monotonically in the single-pulse mode-locked regions. An extremum seeking controller maximizing the energy would climb this function past the largest single-pulse energy solution ($\square$) to the peak energy solution ($\triangle$) which is in the middle of the grey region, and is chaotic. In the second panel of Figure 4.2, we see this chaotic solution ($\triangle$), as well as the fat pulse at the edge of the white region ($\square$), and the desirable tight mode-locked pulse ($\diamond$) that maximizes the

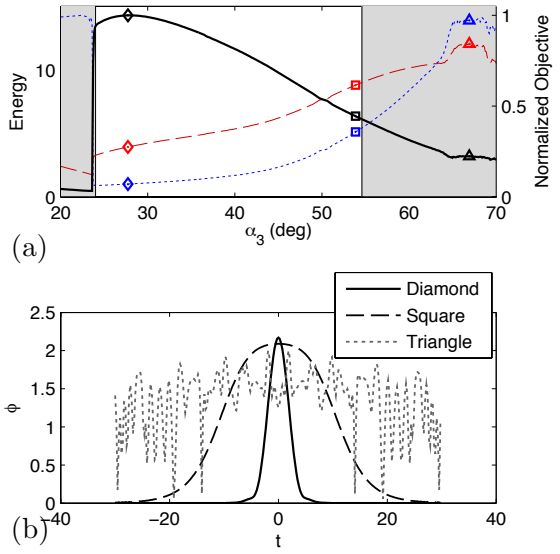

Figure 4.2: Zoom in near peak in objective function (⋄). (a) The objective function (–), energy (- -), and kurtosis (· · ·) versus half-waveplate angle α_3. (b) Energy of the waveforms versus time for the cases shown in diamond (⋄), square (□), and triangle (△). The peak of the objective function (⋄) is a localized pulse, and the peak of the total energy (△) is a chaotic solution.

new objective function. Table 4.2 shows the energy E, kurtosis of the spectrum κ, and the new objective function E/κ for each of these three cases.

Table 4.2: Comparison of three laser states.

	Energy, E	Kurtosis, κ	Objective, E/κ
Tight Pulse, (⋄)	3.9314	17.6153	0.2232
Fat Pulse, (□)	8.7932	88.6002	0.0992
Chaotic, (△)	11.0067	229.2296	0.0480

It is important to note that this objective function is not the only good choice, and others may be more readily determined from experimental measurements. We have chosen an objective function that balances the total energy in a pulse with some measure of the

width of the pulse, which selects for tight mode-locked pulses. However, if a fat pulse is more favorable in a given application, it is possible to construct an objective function for which these waveforms are local maxima. The following control laws will work for any objective function whose local maxima are mode-locked pulses of the desirable shape and characteristics.

4.5 Extremum-Seeking Controller

Extremum-seeking control (ESC) is an adaptive control law that finds and tracks local maxima of an objective function by sinusoidally varying a set of input parameters and measuring the consequent variation of the objective function [27, 32, 43]. The resulting controller does not rely on a model of the dynamics that relate the input parameters to the objective function, making it is especially useful for complex, nonlinear systems with disturbances that are difficult to model. Instead, the measured variation in the objective function is compared with the varying input signal to dynamically improve an estimate of the optimal input parameter. If designed correctly, extremum-seeking is guaranteed to stably converge to a neighborhood of the control input u^* that yields a local maximum of the objective function.

Figure 4.3 shows an extremum-seeking controller for the laser system with a single-input and a single-output (SISO). The input variable is a single polarizer angle, and the output is the objective function E/κ discussed in Section 4.4. The algorithm works by adding a perturbation signal $a\sin(\omega t + \beta)$ to the *best guess* of the input $\hat{u}$ that maximizes the quantity of interest, namely, the objective function. The perturbation passes through the system and results in a perturbation in the output. The high-pass filter of this output is a signal ρ that oscillates about zero mean. Multiplying the high-pass filtered output by the input perturbation yields a *demodulated* signal ξ that is positive when $\hat{u} < u^*$ and negative when $\hat{u} > u^*$. Finally, integrating ξ into our estimate $\hat{u}$ brings the estimate $\hat{u}$ closer to the optimal value u^* corresponding to a local maximum. The input and output sinusoids are plotted with the demodulated signal ξ in Figure 4.4.

There are a number of important considerations when designing an extremum-seeking-controller. First, there are three distinct time-scales of interest in the problem:

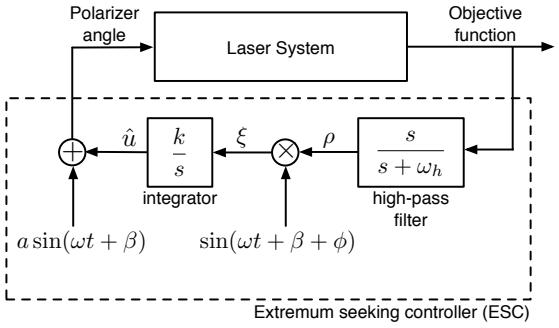

Figure 4.3: Single-input, single-output (SISO) extremum-seeking controller.

1. slow - external disturbances to be rejected,
2. medium - perturbation frequency ω,
3. fast - internal system dynamics.

The perturbation frequency ω must be chosen to be faster than the external disturbances (such as slow changes in birefringence) and slower than the internal system dynamics. For the laser system, the internal dynamics are extremely fast compared with the time it takes to change the polarizer angles.

Next, the amplitude of the perturbation a is chosen sufficiently large so that there is a measurable perturbation in the output of the system; larger a also results in faster convergence to the optimal u^*. However, a should not be so large that there is significant steady-state error due to oscillations about the peak. Faster convergence is also attainable by increasing the integrator gain k, although this will destabilize the system for large enough k. Finally, we choose the cut-off frequency ω_h for the high-pass filter based on the perturbation frequency ω.

Figure 4.5 shows a multi-parameter extremum-seeking controller for the laser system with multiple-inputs, and a single-output (MISO). This consists of a number of separate extremum-seeking loops (labeled ESC 1 through ESC n), each with their own perturbation signal and magnitude, high-pass filter, and integrator. It is generally more involved to

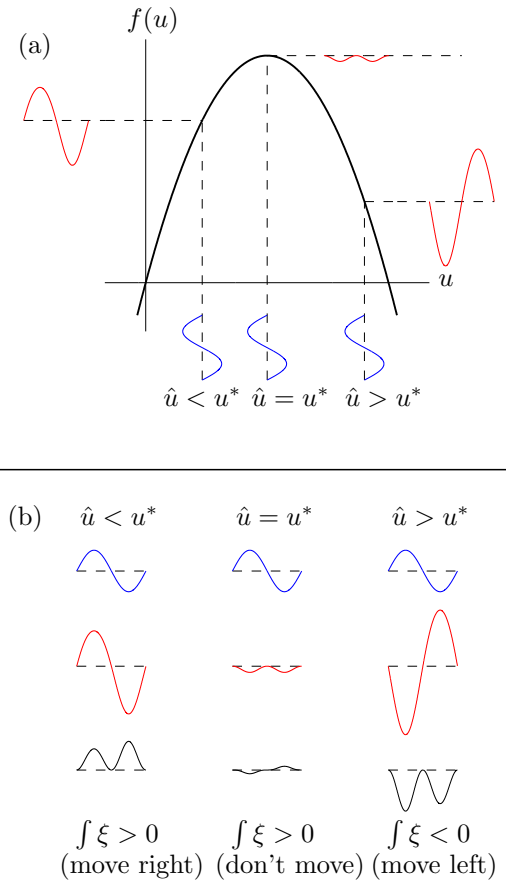

Figure 4.4: (a) Illustration of sinusoidal perturbation to the input $\hat{u}$ near an optimal value u^*. (b) The input and high-pass filtered outputs are multiplied to give the black curves (ξ). If $\hat{u} < u^*$, then ξ is purely positive, and $\hat{u}$ moves to the right towards u^*. Similarly, if $\hat{u} > u^*$ then ξ is purely negative and $\hat{u}$ moves left. When $\hat{u} = u^*$, then the integral of ξ is zero, and $\hat{u}$ doesn't move. Notice that the signal ξ is larger when the slope of the function is larger.

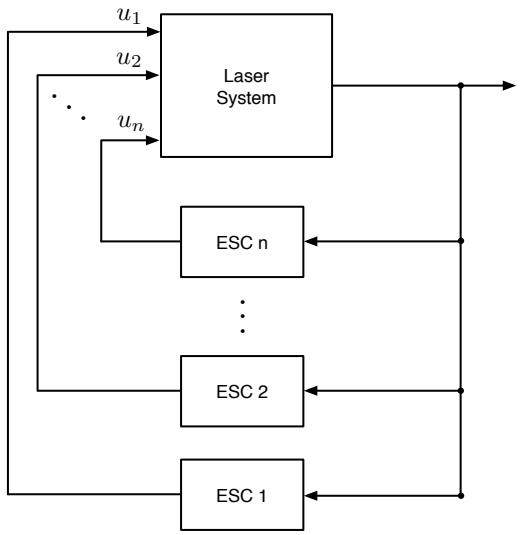

Figure 4.5: Schematic for multiple-input, single-output (MISO) extremum-seeking controller. Each ESC block is a SISO unit as shown in Figure 4.3.

develop a well-tuned extremum-seeking controller for a MISO system, although guidelines for stable controllers do exist [27].

The perturbation frequencies of each extremum-seeking loop must satisfy the following property: $\omega_i + \omega_j \neq \omega k$ for any $i, j, k = 1, 2, \ldots, n$. This protects against the possibility of bias arising from demodulation. It is also possible to use the same perturbation frequency for each pair of even and odd controllers, so that $\omega_k = \omega_{k+1}$ as long as they are out of phase: $\beta_k = 0$ and $\beta_{k+1} = \pi/2$. In practice, we designed each of the single-parameter controllers in isolation and then sequentially combined parameters and refined the design.

It is important to note that the extremum-seeking controller will only find local maxima of the objective function. Therefore, it is important to start with a reasonably good mode-locked solution as the initial condition. One potential way to ensure that good solutions are used in the extremum-seeking controller is to first apply a genetic algorithm to find suitable regions of performance [67]. However, there are also other methods as outlined in the next section.

4.6 Performance of Extremum-Seeking Control

The results in this section demonstrate the utility of extremum-seeking control for the mode-locked laser. In the first two sections, the controller is used to find locally optimal polarizer angles for a fixed birefringence K. In the third section, the controller is used to track a high-energy mode-locked state despite significant variations in birefringence that occur on the order of minutes. This is designed to be a worst-case scenario to demonstrate the high performance of the controller. It is expected that typical disturbances will be more mild, both in terms of amplitude and frequency of disturbances.

Since the extremum-seeking controller only finds local maxima, there are initial conditions that yield poor locally optimal solutions that are not mode-locked. Similarly, drastic perturbations may knock the system far enough from the local maximum that the controller is unable to recover. We envision a start-up routine to select good initial conditions at the beginning of operation and after drastic perturbations, whereby each of the polarizer/wave-plate angles are varied simultaneously at different, incommensurable rates. This strategy has been tested in simulations, and it is possible to find sub-optimal mode-locked solutions very quickly, within a relatively small number of whole revolutions of the slowest angle. From this starting condition, we then turn the extremum-seeking controller on.

There is no guarantee that the extremum-seeking controller will arrive at the same local maximum, given different initial conditions. In fact, it is impossible to tell if the extremum-seeking controller arrives at the globally maximizing solution without a full parametric study, which may be prohibitively expensive. However, the general approach of cycling each control angle at incommensurable rates is guaranteed to pass arbitrarily close to every possible configuration in a finite amount of time without sampling the same condition twice. This provides a powerful and flexible strategy for mapping configuration space. After a favorable mode-locked solution is found, the extremum-seeking controller is turned on to first obtain and then maintain the local maxima, despite disturbances.

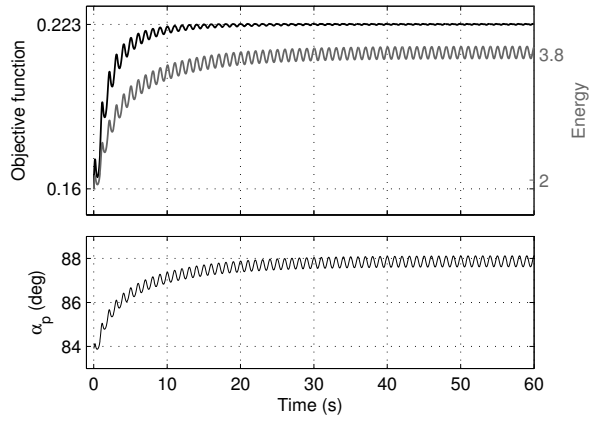

Figure 4.6: Extremum-seeking controller for a single parameter (α_p) with a fixed birefringence, $K = 0.1$.

4.6.1 Single-Parameter Extremum-Seeking Control for Fixed Birefringence K

Figure 4.6 shows the extremum-seeking controller for a single-input, single-output (SISO) case. The polarization angle α_p is the control variable. Both the objective function and the energy rise from the initial value as the controller tracks the (locally) optimal parameter value. Steady-state tracking is achieved within approximately 30 seconds. Although the input parameter continues to oscillate after the extremum is found, the oscillations in the objective function are quite small since the first derivative is zero at the peak. The parameter values of the extremum-seeking controller used in Figure 4.6 are given in Table 4.3.

Single-parameter extremum-seeking control has also been simulated numerically for the other waveplate angles, α_1, α_2, and α_3 independently, and the results are qualitatively the same as Figure 4.6. In experiments, the presence of sensor noise may motivate an increase in the amplitude of oscillation a, a decrease in the frequency of oscillation, or both. Time delays τ in the sensing and actuation may be incorporated into the phase delay ϕ according to the formula $\phi = \tau\omega$ so that the high-pass filtered measurement and input perturbation are aligned. Note that there is no convergence criterion, after which the controller is shut off; even after it converges on the local maximum, the controller continues to adaptively correct for slow disturbances.

Table 4.3: Extremum-seeking parameter values (single-input)

	ω (rad/s)	β (rad)	ϕ (rad)	a (deg)	ω_h (rad/s)	k
α_p	2π	$\pi/2$	0	0.5	2π	10

Table 4.4: Extremum-seeking parameter values (multi-input)

	ω (rad/s)	β (rad)	ϕ (rad)	a (deg)	ω_h (rad/s)	k
α_1	1.2π	0	0	0.5	2π	5
α_2	4.512π	$\pi/2$	0	0.5	2π	50
α_3	2π	0	0	0.5	2π	50
α_p	2π	$\pi/2$	0	0.5	2π	20

4.6.2 Multi-Parameter Extremum-Seeking Control for Fixed Birefringence K

Figure 4.7 shows the extremum-seeking controller for the multiple-input, single-output (MISO) case where we are controlling all four polarizer angles simultaneously. The extremum-seeking control parameters are shown in Table 4.4. The multi-parameter design is more complicated than the single parameter case, and involves first designing single-parameter controllers and then combining them pairwise and modifying until the desired performance is achieved.

The multi-parameter extremum-seeking controller takes longer to converge to a local maximum than the single-parameter case, approximately 2 minutes as opposed to 30 seconds. There are two main reasons for this slower convergence: 1) the angle α_1 is being oscillated more slowly, and 2) as the angles are varied simultaneously, they affect each other, and larger overall excursion of the angles is required to reach the maximum. Because

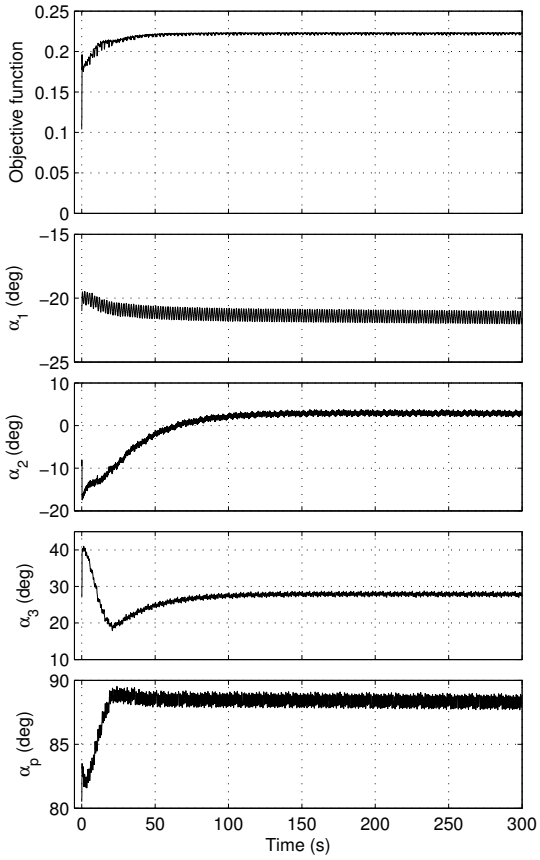

Figure 4.7: Multi-parameter extremum-seeking controller with a fixed birefringence, $K = 0.1$.

parameters are all being varied simultaneously at incommensurable rates, occasionally there will be a large excursion in each of the angles, resulting in a large radius in parameter space from the optimal values. Since the mode-locked state is sensitive to large amplitude excursions to the input angles, this may present a challenge to incorporate more input parameters into the extremum-seeking control algorithm.

Finally, it is important to note that for this particular configuration, the extremum-seeking controller performance is sensitive to the control parameters for the α_1 variable. The oscillation frequency for α_1 is chosen to be the slowest frequency and the gain k is also the smallest among the input angles. If either of these values are increased significantly, then the controller may get stuck in a periodic-orbit configuration where the variable α_1 precesses at a slow rate, while the other variables rapidly adjust to compensate. Although this is not shown, it is quite interesting that during this precession, the objective function remains relatively constant, suggesting that there are a family of favorable mode-locked states parameterized by α_1. In practice, this might suggest that the variable α_1 is redundant, which is the subject of current investigation.

4.6.3 Multi-Parameter Extremum-Seeking Control for Varying Birefringence K

Figure 4.8 shows the objective function and energy for a range of birefringence K for a set of fixed input angles; the angles are chosen to (locally) maximize the objective function at $K = 0.1$ as in Figure 4.7. On either side of $K = 0.1$ the objective function decreases, although there is a steep drop-off for larger positive values of K, corresponding to the loss of mode-locking.

In Figure 4.9 we vary the birefringence K according to a large-amplitude saw-tooth pattern (left) and according to a pseudo-random walk (right). In each of these cases, the extremum-seeking controller is compared with the case when no control is applied and the polarizer angles are fixed at the optimal values for $K = 0.1$. For both aggressive K disturbances, the extremum-seeking controller maintains a high-energy mode-locked state, although the uncontrolled system frequently loses mode-locking. It is interesting to note that the fourth input parameter, α_p tracks the K disturbance nearly linearly. The objective

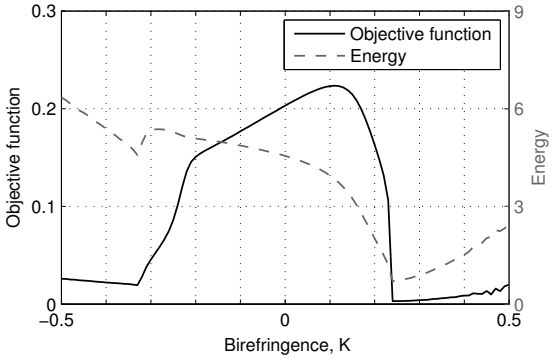

Figure 4.8: Energy and objective function vs. birefringence, K.

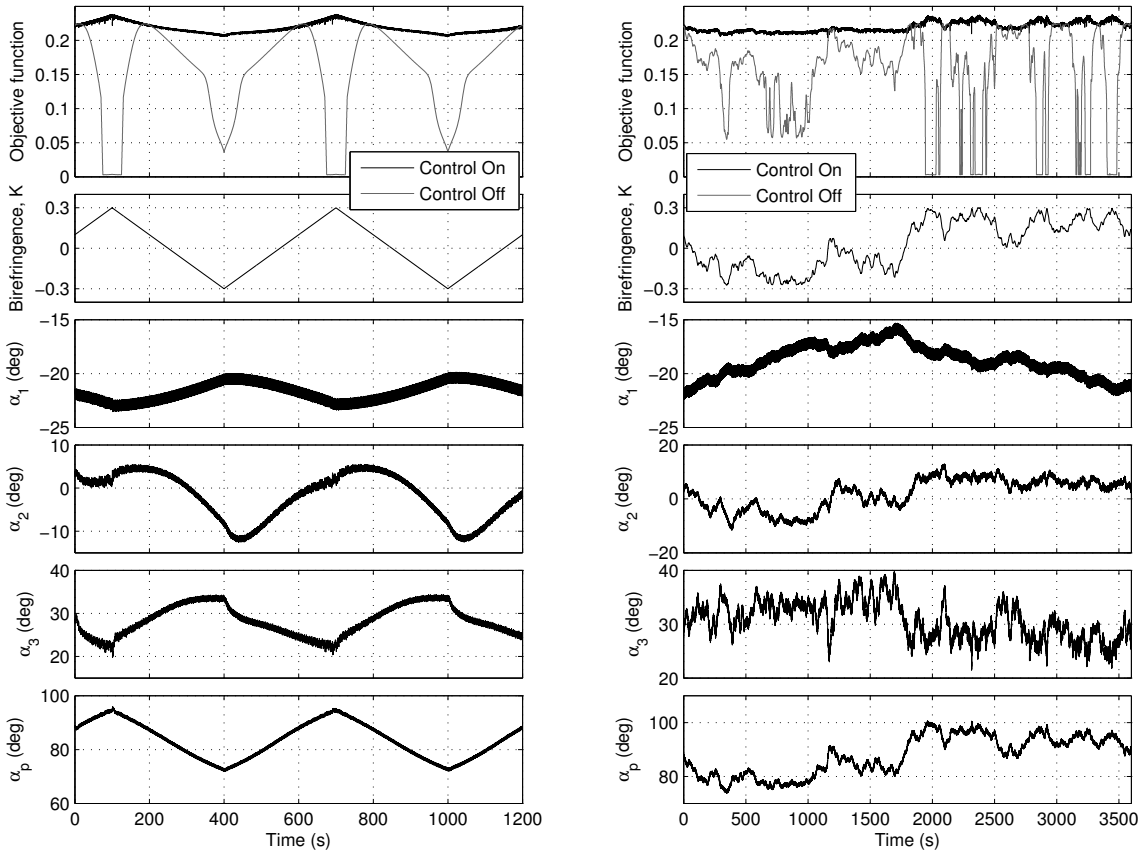

Figure 4.9: Multi-parameter extremum-seeking controller with a varying birefringence, K. (left) The birefringence varies as a sawtooth function, and (right) the birefringence varies according to a pseudo random walk.

function fluctuates slightly in the case with controller, since the local maximum value varies with the birefringence K.

As noted in Table 4.2, the quality of the mode-locked pulse is significantly degraded for an objective function value near 0.1, and the solution is fully chaotic near 0.05. Thus, without control, the laser performance is severely effected by variations in birefringence.

4.7 Summary

We have developed a fast, stable extremum-seeking controller for the passively mode-locked fiber laser based upon NPR. The controller simultaneously varies the four angles corresponding to waveplates and polarizer in a single-NPR laser to maintain a high-energy mode-locked state despite large, rapid changes in the birefringence K. The amplitude and frequency of the disturbance are chosen to be more aggressive than expected values, demonstrating that the controller successfully rejects disturbances in a worst-case scenario.

A new objective function was developed for use with the multi-parameter extremum-seeking controller. This objective function divides the energy of a solution by the kurtosis of the Fourier spectrum of the waveform. There are two main criteria for this objective function: 1) high-energy mode-locked states appear as local maxima of the objective function with a buffer between the maxima and chaotic or multi-pulse regions, and 2) it is expressed in terms of experimentally measurable quantities. The objective function developed in this work is not necessarily the only or best function. We might also incorporate quantities such as the average power, full-width at half-maximum of the pulse, or autocorrelation into another objective function depending on specific design goals. It is also possible to use high-frequency sampling to time-average and reduce measurement noise in experiments.

Chapter 5

SPARSITY AND LIBRARY BUILDING FOR COMPLEX SYSTEMS

5.1 Overview

It has been observed that changes in the birefringence, which are difficult or impossible to directly measure, can significantly affect mode-locking in a fiber laser. In this chapter[1] we develop techniques to estimate the effective birefringence by comparing a test measurement of a given objective function against a learned library. In particular, a toroidal search algorithm is applied to the laser cavity for various birefringence values by varying the waveplate and polarizer angles at incommensurate angular frequencies, thus producing a time-series of the objective function. The resulting time series, which is converted to a spectrogram and then dimensionally reduced with a singular value decomposition, is then labelled with the corresponding effective birefringence and concatenated into a library of modes. A sparse search algorithm (L_1-norm optimization) is then applied to a test measurement in order to classify the birefringence of the fiber laser. Simulations show that the sparse search algorithm performs very well in recognizing cavity birefringence even in the presence of noise and/or noisy measurements. Once classified, the wave plates and polarizers can be adjusted using servo-control motors to the optimal positions obtained from the toroidal search. The result is an efficient, self-tuning laser.

5.2 Introduction

Mode-locked fiber lasers have continued to make tremendous strides in engineering performance, both in terms of output energy and peak powers, yielding approximately a two orders of magnitude power increase in the last decade [1]. Despite such exceptional experimental achievements, first-principals modeling of fiber lasers has remained, for over two decades now, *qualitative* in nature. The underlying and primary reason which has pre-

[1] Content of this chapter is published in journal article [69].

vented *quantitative* modeling efforts is the fiber birefringence [25, 26, 63, 64] (See also the recent review article by Gordon and Kogelnik [65]). It is well understood from these studies, primarily aimed at fiber optic communications, that the fiber birefringence is stochastic in nature, varying randomly along the length of the fiber laser cavity and highly susceptible (and sensitive) to environmental factors such as bend, twist, anisotropic stress, and ambient conditions such as temperature. With modern data-analysis methods, we propose to optimize mode-locking performance by learning a proxy measure and classification for the fiber birefringence, thus allowing for a self-tuning laser design capable of adapting rapidly to changes in birefringence.

Just as in optical communications, a fiber laser cavity propagates pulses over ultra-long distances in fractions of a second. Signal distortions due to the chromatic dispersion and nonlinearity accumulate after many round trips of the laser cavity, as does the signal distortion due to the fiber birefringence [25, 26, 63–65]. Successful pulsed laser operation is achieved when the linear and nonlinear cavity effects balance each other resulting in stable mode-locked pulses [2, 66]. Although single-mode fibers are typically used for such laser cavities, the so-called single-mode fibers in fact support two modes simultaneously, which are orthogonally polarized. In an idealized circular-core fiber, these two modes will propagate with the same phase velocity. However, practical fibers are not perfectly circularly symmetric. As a result, the two modes propagate with slightly different phase and group velocities due to small differences in the effective index of refraction experienced by each. While this birefringence is small in absolute terms in standard optical fibers, approximately 10^{-7} index of refraction difference in the two modes, the corresponding beat length L_B is about 10 meters with variations occurring on lengths of 100 meters, which is often on the same order as the dispersive and/or nonlinear length scales. As a result, the birefringence can have a significant impact on mode-locking dynamics.

To illustrate the cavity sensitivity to birefringence, consider one of the most commercially successful mode-locked lasers to date (See Fig. 5.1): the well-known mode-locked fiber laser that relies on nonlinear polarization rotation (NPR) for achieving saturable absorption using a combination of waveplates and polarizer [2–5]. This NPR based laser concept is more than two decades old and is so successful in part due to its reliance on simple off-the-shelf

telecom components, rendering it a highly cost-effective mode-locking source. More recently, tremendous performance advances in this NPR laser have been made in power delivery by using all-normal dispersion fiber cavities [**?**, **?**, 9] and/or self-similar pulse evolutions [6–8]. It has also been recently conjectured that multi-NPR sections can be used in the cavity to overcome the multi-pulsing instability and achieve additional performance gains [13, 20, 67]. However, such commercial lasers must enforce strict environmental control to maintain performance, i.e., the fiber birefringence is controlled by pinning into place and shielding it from temperature fluctuations. Such system sensitivity has prevented it from major performance advances, limiting power and pulsewidths. Moreover, failure to accurately model the stochastic and sensitive birefringence fluctuations in the cavity have deprived the community for more than two decades of a quantitatively accurate model of this highly successful laser system.

Our objective in this chapter is to make use of modern data-analysis methods, i.e. machine learning techniques, to help discover a proxy measure for the effective cavity birefringence. Unlike optical communication lines where over long distances a statistical average might be experienced by a pulse, here a single realization of a stochastic variation of the birefringence is what drives the laser cavity dynamics (See Fig. 5.1(c)). If the cavity is perturbed by bend, twist, anisotropic stress, and/or ambient temperature, then a new realization results. For optimizing performance, it is critical to characterize, or recognize, the fiber birefringence correctly in order to determine the waveplate and polarizer settings, for instance, required to give the best energy performance.

Using pattern learning methods, we demonstrate that spectrogram measurements, which are dimensionally reduced using a singular value decomposition, uniquely characterize the average cavity birefringence. This gives rise to a sparse representation and classification scheme for identifying the dynamic regime of the cavity. Our algorithm allows for efficient self-tuning of the laser cavity when combined with an adaptive controller [68] with servo-driven components [23,70]. Thus instead of attempting to model the stochastic birefringence fluctuations directly, which can only practically be done in a statistical way, we instead measure and learn the impact of birefringence on mode-locking performance and provide a method by which optimal, self-tuning can be achieved. Although we demonstrate the

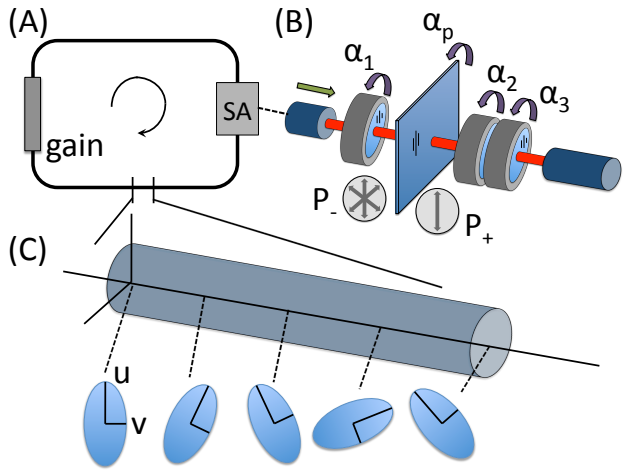

Figure 5.1: (A) Schematic of a mode-locked laser cavity which includes a ring fiber with saturable absorber (SA) and gain element. (B) The SA is generated by nonlinear polarization rotation interacting with three waveplates (α_j where $j = 1, 2, 3$) and a polarizer (α_p). Incoming polarized light (P_-) is attenuated by the polarizer if it is not in alignment with the transmitting axis. Thus only a single polarization direction (P_+) is transmitted. (C) The fiber itself is subject to stochastic fluctuations in the birefringence, i.e. random rotations of the principal fast- and slow-axes, u and v respectively. Shown is an example portion of fiber where the rotations depend sensitively on bend, twist, anisotropic stress, and/or ambient temperature.

method on a computational model, the algorithm would ideally apply directly to the laser cavity as there is no need for an underlying model.

The chapter is outlined as follows: Sec. 2 outlines the theoretical (computational) model used for the laser cavity along with the adaptive controller and objective function for optimizing the cavity performance. Section 3 develops a toroidal search algorithm which allows for an extensive and rapid search of the best candidate mode-locked states in the system. The construction of spectrograms for various average birefringence values are also shown. Section 4 develops the primary contribution of the chapter: an algorithm that is capable of recognizing the average birefringence state of the system. Key to an accurate recognition is the application of a sparse classifier, which is a novel method for identifying dynamical regimes. Section 5 gives the results of the classification methodology and shows the success of the algorithm. An overview of the method and future outlook of its applicability are given in the concluding Sec. 6.

5.3 Fiber Laser Model and Objective Function

In previous work [68], an extremum seeking controller (ESC) was designed to achieve and maintain a high-energy, single-pulse state in a mode-locked fiber laser. Given initial parameter values, the ESC enables us to obtain the local maximum of our objective function by varying the fiber laser control parameters, i.e. waveplates and polarizers for a cavity based upon nonlinear polarization rotation. However, the performance of the laser is still limited since the controller itself is only capable of tracking the *local maximum* of the objective function instead of the desired *global maximum*. As a result, we propose a data-driven technique which allows us to build a library of time series of the objective function that globally samples the entire parameter space for different birefringence values. Once a sufficiently large library is obtained, the state of fiber laser system can be then characterized by matching the current system behavior with library entries, hence the global optimal performance can be identified, and then subsequently maintained by ESC. In order to perform such a task, an example model laser system is introduced.

5.3.1 Laser Cavity Model and Objective Function

In order to demonstrate that the machine learning algorithm provides us with the accurate birefringence characterization, full simulations of a laser cavity are performed. In practice, the algorithm advocated here would sample from the experimental laser dynamics and no theoretical model would be required.

To describe the propagation dynamics in the laser fiber, including the interaction of chromatic dispersion, self-phase modulation, birefringence, cavity attenuation/loss, and bandwidth limited gain and saturation, we use the coupled nonlinear Schrödinger equations (CNLS) [25, 26] together with Jones matrices, please see section 2.1.2 for details.

For any sampling and machine learning method to work, one need to decide how to characterize the state of the laser system effectively. In previous work [68](also see Chapter4), an objective function O was introduced which was obtained by dividing the pulse energy E by the spectral kurtosis M_4 (fourth-moment) of the wave form:

$$O = \frac{E}{M_4}. \tag{5.1}$$

This objective function, which has been shown to be successful for applying adaptive control, is large (optimal) when we have a large amount of energy in a tightly confined temporal wave packet [68]. The spectral kurtosis M_4 measures the spread of the waveform.

The objective function enables us to discriminate multi-pulse and chaotic wave forms from the desired single-pulse wave form while providing us with a quantity that favors tight, high-energy, single-pulse wave forms. Figure 5.2(h) shows the normalized objective function (red), pulse energy (black) and kurtosis of the spectrum (blue) when rotating on the 2-torus of waveplate α_3 and polarizer α_p. The objective function selected is ideal for optimizing pulse energy while simultaneously keeping the mode-locking away from instability boundaries (gray regions) [68]. Figure 5.2(g) shows the wave forms that correspond to the settings marked by the circle, square, diamond, and triangle in Fig. 5.2(h). The maximal energy occurs away from the regions of single-pulse mode locking (white region), thus tracking energy alone as the objective function would lead to chaotic solutions (grey regions). In contrast, the objective function has local maxima in the single-pulse, mode-locked region. The spectral kurtosis (blue) is small in the single-pulse mode-locking region and is much larger in the

grey regions because of multi-pulsing or chaotic wave forms. As a result, dividing energy by the spectral kurtosis penalizes non-mode-locked and multi-pulsing mode-locked states. In the remainder of this chapter, we will use this objective function to characterize the state of the fiber laser. It should be noted, however, that any objective function could be picked so that the shortest pulse, broadest spectrum or some other quantity of interest can be selected as a quantity of interest.

5.4 Toroidal Search and Library Building

In this section, a search algorithm will be developed for characterizing the optimal mode-locking performance as a function of birefringence. In practice, this algorithm could take a few to tens of minutes to execute given the fact that mode-locking itself occurs in microseconds. Thus the only limitation to how fast the algorithm can be executed is the speed of the servo-driven controllers [23, 70].

5.4.1 Toroidal Search

In the experimental setting, the NPR unit consists of the polarizer and three waveplates that can be rotated from 0 to 2π, thereby creating a parameter space that is a 4-torus. Multiple NPR sections can be included, let's say N of them, to further enhance performance [13, 20, 67]. In order to sample the resulting parameter space ($4N$-torus), a toroidal search algorithm is developed. If we want to sample this $4N$-dimensional torus, then $4N$ time series are constructed from:

$$\theta_j(t) = \omega_j t + \theta_{j0} \tag{5.2}$$

for $j \in [1, \ldots, 4N]$, where θ_{j0} are initial parameter values, ω_i are angular frequencies which are incommensurate, i.e. equation

$$m\omega_j + n\omega_k = 0 \tag{5.3}$$

doesn't have integer solution. In other words, ω_j/ω_k is irrational for any $j, k \in [1, \ldots, 4N]$, given $j \neq k$. It is easy to prove that under such conditions, $[\theta_1(t) \ \ldots \ \theta_{4N}(t)]$ is dense on the torus [71]. Thus using this method, it is guaranteed that one can sample any torus

sufficiently well if sampling for a long enough time or using a high enough sample rate. In the following sections of this chapter, we take a 2-torus for a single NPR laser as a simple example case. However, the methods mentioned in this chapter can be applied to toroidal parameter spaces of any dimensionality. Figure 5.2 shows how the toroidal sampling works on a 2-torus comprised of parameters α_3 and α_p. Specifically, the resulting time series of the objective function O is demonstrated as the 2-torus is sampled. In Fig. 5.2(a), the torus in under-sampled and aliasing of the objective function occurs. However, as the sampling rate is increased, as shown in Fig. 5.2(e), the objective function is fully constructed and an evaluation of best performance can be ascertained. Indeed, the red dot in Fig. 5.2(f) shows the optimal global maxima of the laser cavity. The narrow shaded region around this peak performance is highlighted in Fig. 5.2(h) where an additional evaluation is made of whether the solution is mode-locked or not.

5.4.2 The Gábor Transform (spectrogram) and Library Building

For a given birefringence value, toroidal sampling is used to produce a time series of the objective function. Note that we use the entire time series to compute spectrograms in our library building process. Once the library is constructed, optimal parameter settings are kept for future use. In order to develop a robust algorithm that matches the current objective function time series with the library entries, we want to utilize both the temporal and spectral (frequency) signatures of the time series. As a result, we introduce the Gábor transform and construct a spectrogram [80] of the optimal solution.

It is observed that the time series collected from toroidal sampling are comprised of various frequency components that are exhibited at different times. Although the Fourier transform of the signal contains all frequency information, there is no indication of when each frequency occurs in time. Indeed, by definition, the Fourier transform eliminates all time-domain information since we integrate over all time. To circumvent the limitation of the direct application of Fourier transform, Gábor proposed a formal method for keeping information in both time and frequency. His method involved a simple modification of the

Fourier transform kernel:

$$g_{t,\omega}(\tau) = e^{i\omega\tau} g(\tau - t), \tag{5.4}$$

where the filter $g(\tau - t)$ was introduced with the aim of localizing both time and frequency. The Gábor transform, also known as the short-time Fourier transform is then defined as:

$$\tilde{f}_g(t, \omega) = \int_{-\infty}^{\infty} f(\tau)\bar{g}(\tau - t)e^{-i\omega\tau} d\tau, \tag{5.5}$$

where the bar denotes the complex conjugate of the function. Thus the function $g(\tau - t)$ acts as a time filter for localizing the signal and its frequency content over a specific window of time, allowing for the construction of a spectrogram. A spectrogram represents a time series (signal) in both the time and spectral domain, as shown in Fig. 5.3.

Our key observation is that these spectrograms are unique for varying cavity birefringence. Thus the spectrogram serves as a proxy measure for classifying the underlying cavity birefringence. Unique spectrograms for various birefringence values in the library are shown in Fig 5.4. By definition the spectrograms are symmetric in frequency, for storage and computation efficiency concerns, we only use the positive frequency part of the spectrograms for classification purposes. These spectrograms serve as the basis of a pattern recognition/classification scheme for determining the value of cavity birefringence.

5.5 Birefringence Classification and Recognition

In the previous section, we built a spectrogram library using a Gábor transform with Gaussian window. To match a current time series with library entries, the Gábor transform is also applied to the time series sampled from the current system to get the spectrogram. A sparse sampling technique is then applied to recognize the current birefringence from possible library elements.

To start, assume we have computed the spectrogram S_k for a large number of possible birefringence values where k ranges from 1 to M, and for each k, a singular value decomposition (SVD) is applied to the spectrogram [80]:

$$S_k = U_k \Sigma_k V_k^* \tag{5.6}$$

and

$$U_k = [u_{k_1} u_{k_2} \cdots u_{k_n}]. \tag{5.7}$$

For each k value, we keep the first m ($m < n$) modes (low-rank approximation) of U_k which has the highest energy and store them in the modes library U_L such that

$$U_L = [\tilde{U}_1 \tilde{U}_2 \cdots \tilde{U}_M] \tag{5.8}$$

where the k-th sub-library $\tilde{U}_k$ contains the first m modes of U_k:

$$\tilde{U}_k = [u_{k_1} u_{k_2} \cdots u_{k_m}]. \tag{5.9}$$

Once we have constructed our dimensionally reduced modes library, we can take a measurement of the laser system (the objective function) and compute the spectrogram. Note that the sampling time does not have to be of the same length as the time series collected when the library was built. We perform an SVD reduction on the measured spectrogram and keep the first m modes as before, as illustrated in Fig. 5.5. With the most important (dominant) modes from the measurement in hand, we can do an L_1-norm library search, thus promoting sparsity in our solution [80]. In the L_1-norm search, our objective is to find a vector

$$a = \arg\min_a \|a\|_1 \tag{5.10}$$

subject to

$$U_L \cdot a = u_{m_1}\,. \tag{5.11}$$

Here we require the number of library modes to be greater than the dimensionality of the frequency domain. Given this condition, this becomes an underdetermined linear system of equations. The L_1-norm minimization produces a sparse vector a, i.e. only a small portion of the elements are non-zero, as shown in Fig. 5.6. The non-zero elements of vector a act as a classifier (indicator function) for identifying which sub-library the birefringence falls into. Thus if the largest element falls into the i-th sub-library, the recognized birefringence value is equal to K_i. This sparsity promoting optimization, when used in conjunction with the unique spectrograms, gives a rapid and accurate classification scheme for the fiber birefringence. Thus birefringence recognition can be easily accomplished. Note that our classification scheme essentially uses the L_1-norm minimization produce as an indicator function for

the correct library elements. More sophisticated sparse classification/recognition strategies can be applied if desired [72], potentially yielding even better recognition results.

5.6 Classification Results

The sparse search algorithm is tested using the pre-computed spectrograms with Gaussian random noise added. In our test, the birefringence K is varied following a gaussian random walk. For each trial, the spectrogram corresponding to the current birefringence is computed and the L_1-norm sparse search is executed. Recognition results and errors are showed in Fig 5.7. In the figure, the recognition algorithm is tested in two scenarios: (i) well-aligned data given the assumption that the servo motors that control the waveplates and polarizers work without error, and (ii) the mis-aligned data that considers the error in the initial angle of the servo motors. In both of these two scenarios, the sparse search works very well. In the well-aligned case, a birefringence recognition (classification) rate of 98% is achieved while in the mis-aligned case, we get a 88% recognition rate. It should also be noted that even when our recognition algorithm fails to find the correct birefringence value, the error between the true birefringence and the recognized value is very small. Thus, even if we use the mis-classified birefringence, is is likely that the predicted optimal parameters will be near the true optimal parameters and the adaptive controller [68] will bring the laser system back to peak performance.

5.7 Summary

The stochastic nature of fiber birefringence has been the major impediment in allowing for *quantitatively* accurate modeling of fiber lasers for optimizing their performance. Indeed, all other physical parameters in the system, such as the Kerr nonlinearity, dispersion characteristics as a function of wavelength, gain and gain bandwidth, can be fairly well characterized in theoretical models. Thus only the birefringence remains unknown and randomly varying. And unlike optical communications, where statistical averaging methods can be used to quantify its effects statistically, a fixed laser cavity represents a single, and unknown, statistical realization of the birefringence which is highly susceptible and sensitive to environmental factors such as bend, twist, anisotropic stress, and ambient conditions

Algorithm for Training and Execution	
1. Toroidal Search for Different K	
- start search with same initial value	`theta_0_vec %initialization`
- generate time series for toroidal search	`theta_vec(t)=omega_vec*t+theta_0_vec`
- collect corresponding objective function	`objfun(k,t)=obj_calc(theta_vec(t))`
2. Library Building	
- compute spectrogram†	`S_k=spectrogram(objfun(k,t))`
- SVD† each spectrogram†	`[U_k,Sigma_k,V_k]=svd(S_k)`
- keep first m modes	`U_tilde_k=U_k(:,1:m)`
- store SVD modes in library	`U_L=[U_L,U_tilde_k]`
3. Sparse Representation Recognition	
- compute spectrogram† (current)	`S_curr=spectrogram(Obj_curr)`
- SVD† spectrogram	`[U_curr,Sigma_curr,V_curr]=svd(S_curr)`
- keep first m modes	`U_tilde_curr=U_curr(:,1:m)`
- $L-1$ norm library search	`K_curr=L1search(U_tilde_curr,U_L)`
- use optimal parameter values based on library	`tmax = find(max(objfun(K_curr,t)),t)`
	`theta_opt = omega_vec*tmax+theta_0_vec`

Table 5.1: Algorithms and pseudo code for training and execution of machine learning module in Fig 5.8. († represents built-in MATLAB functions `svd` and `spectrogram`. The L-1 norm library search can be implemented using the `cvx` package with details provide in Section 4, or with the compressive sampling matching pursuit (CoSaMP) [73].)

such as temperature. Such a system requires new modeling methods which are based upon state-of-the-art data-driven strategies.

We have demonstrated that a toroidal search method forms the basis of a machine learning algorithm for characterizing the performance of a mode-locked laser cavity as a function of birefringence. By constructing a library of objective function spectrograms and their peak performance, a unique signature is given for various cavity birefringence values. Indeed, each unique spectrogram can be reduced using a singular value decomposition and stored in a library for future reference and classification. To evaluate the current cavities birefringence, a time-series sample of the objective function is taken, converted to a spectrogram, reduced using a singular value decomposition, and classified using a sparsity promoting L_1-norm optimization routine. Accuracies as high as 98% are achieved, thus suggesting the algorithm is highly promising for application purposes. And even when birefringence is misclassified, the results are only off by a small percentage, thus suggesting that cavity tuning can still be effective and efficient. Although the algorithm was demonstrated on an underlying theoretical model, the method can be integrated directly into an experimental laser cavity design, i.e. the advocated method does not rely on an underlying model of the laser dynamics.

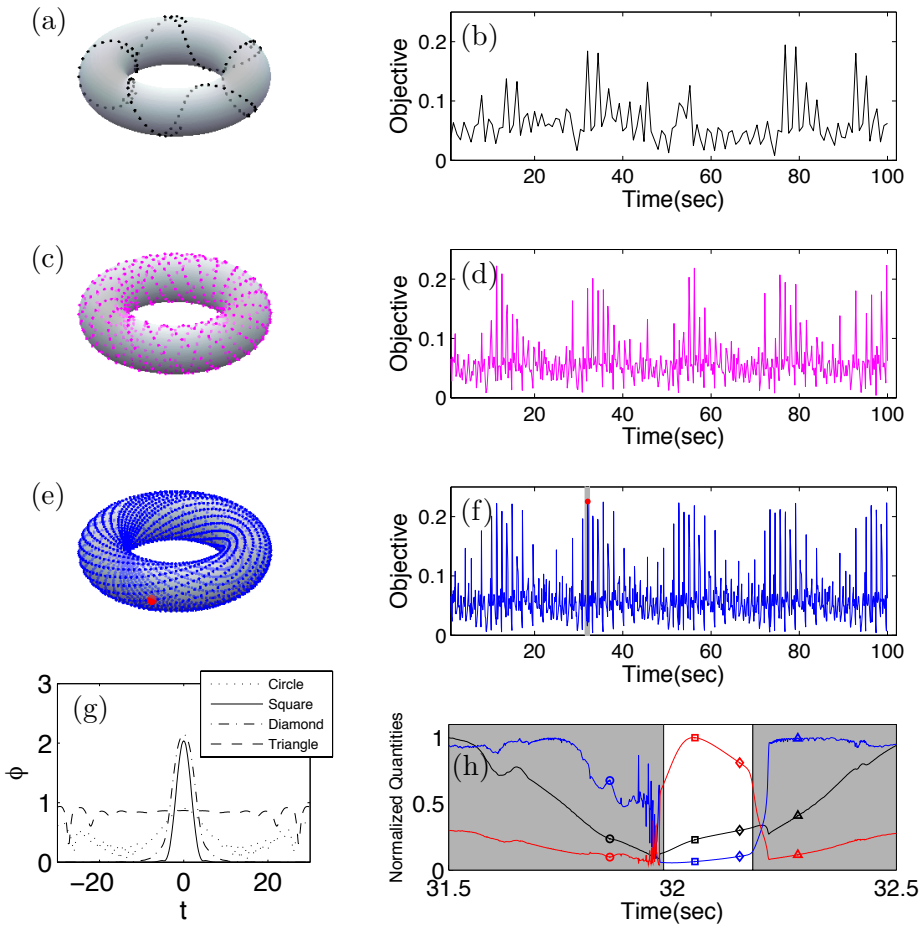

Figure 5.2: (a, c, e) 2-torus of α_3 and α_p with sample points shown (dots) for different sample rates (1.25Hz-black, 5Hz-magenta, 20Hz-blue, the global optimum is marked in red). (b, d, f) The time-series of the corresponding objective function with the global optimum again marked in red. (g) Wave forms of the laser output corresponding to different parameter values marked in (h). (h) Zoomed in objective function (red) plot near the global optimum, pulse energy (black) and kurtosis (blue) are also shown (all normalized to the same scale for comparison).

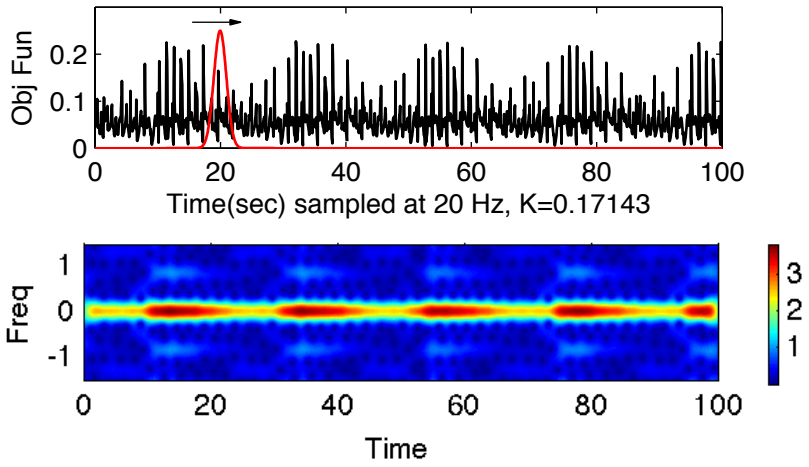

Figure 5.3: Top: objecive function time series sampled at $K = 0.17143$ (black solid), a Gaussian Gábor window centered at $\tau = 20$ is also shown (red solid). Bottom: corresponding spectrogram obtained using Gábor transform with the Gaussian window shown in top panel.

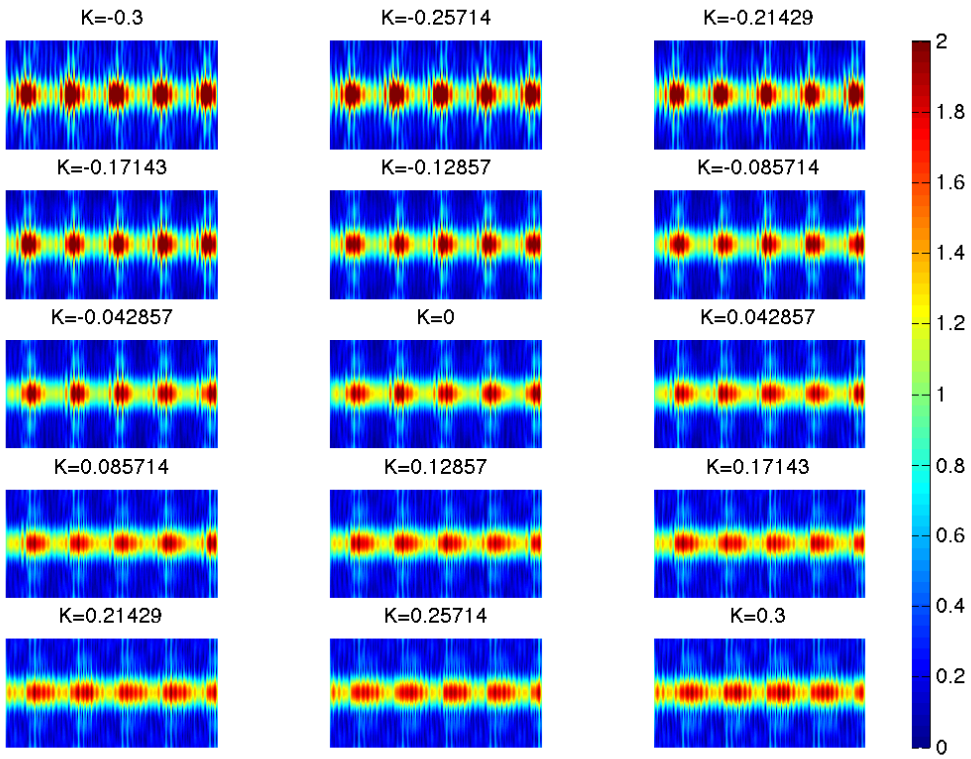

Figure 5.4: Spectrograms for different birefringence values, various (and unique) temporal dynamics can be observed from the comparison.

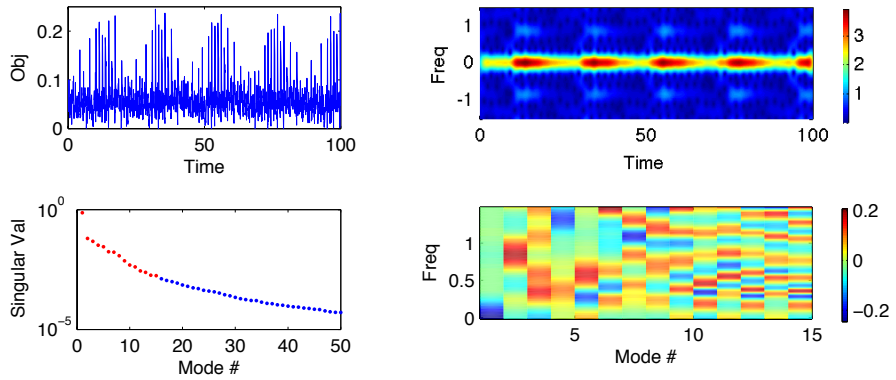

Figure 5.5: Top left: Time series of objective function obtained by toroidal search, sampled at 20Hz. Top right: Spectrogram of the time series. Bottom left: Singular values from SVD, the largest 15 singular values (corresponding to SVD modes used in the library) are plotted in red and the rest are plotted in blue. Bottom right: SVD modes correspond to the largest 15 singular values.

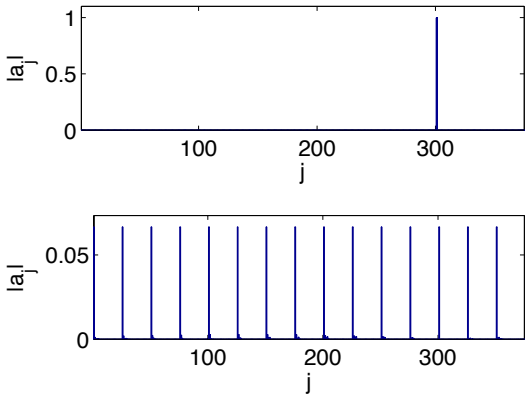

Figure 5.6: Top: Barplot of the components of vector a from L_1 optimization where sparsity can be observed, i.e. it is mostly comprised of zeros. The indicator function nature of the sparse representation is clearly observed. Bottom: Barplot of components of vector a from L_2-norm optimization, showing it does not produce any classification.

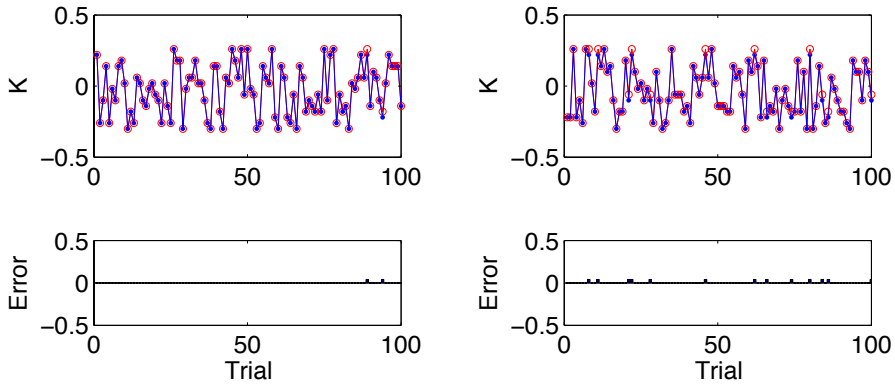

Figure 5.7: Left: Recognition results and errors using well-aligned data. A 98% correct birefringence classification is achieved. Right: recognition results and errors using misaligned (shifted) data. In this case, an 88% correct birefringence classification is achieved. Note that the blue dots represent the true birefringence labels while the red circles are the classified birefringence. Even if misclassified, the algorithm produces a birefringence that is only slightly off, thus still allowing for a rapid tuning of the laser cavity to the optimal waveplate and polarizer settings.

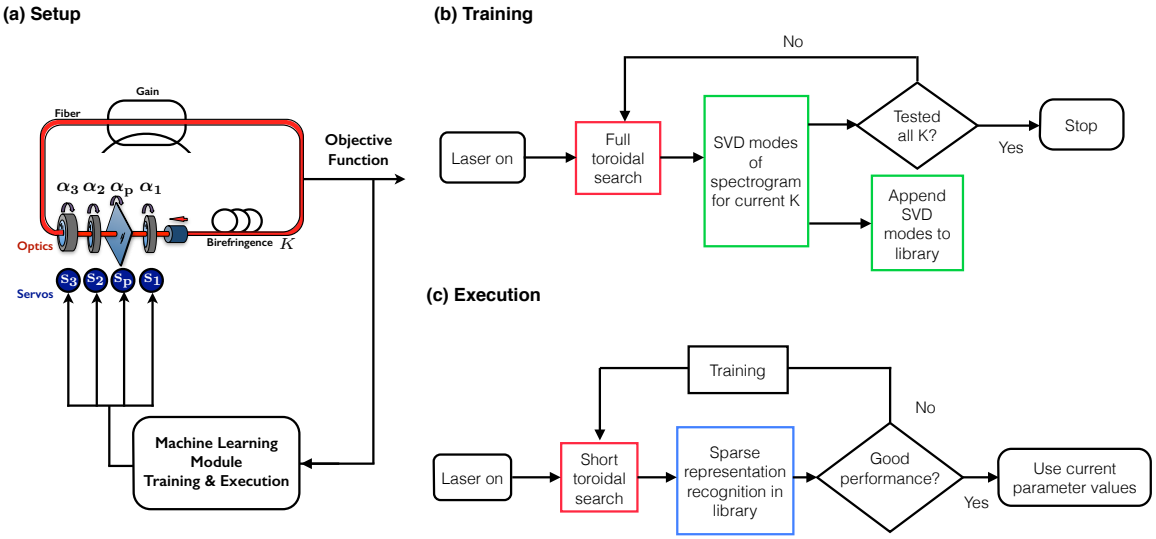

Figure 5.8: (a) Setup of the proposed mode-locked fiber laser wrapped with servos and machine learning module. (b) Flowchart of training algorithm. (c) Flowchart of execution algorithm. Colored boxes have corresponding pseudo code provided in Table 5.1.

Chapter 6

ADAPTIVE DIMENSIONALITY-REDUCTION FOR TIME-STEPPING

6.1 Overview

In this chapter, a numerical time-stepping algorithm for differential or partial differential equations is proposed that adaptively modifies the dimensionality of the underlying modal basis expansion. Specifically, the method takes advantage of any underlying low-dimensional manifolds or redundancy manifest in the system by using dimensionality-reduction techniques, such as the proper orthogonal decomposition, in order to adaptively represent the solution in the optimal basis modes. The method can provide significant computational savings since the reduction can lower the dimensionality of the underlying complex system by orders of magnitude. A comparison of the computational efficiency and error for this method are given showing the algorithm to be potentially of great value for complex systems simulations, especially where slow-manifold dynamics are known to arise.

6.2 Introduction

Computation is ubiquitous across the physical, biological and engineering sciences, revolutionizing many fields of study by allowing one to solve complex problems through algorithmic/numerical methods. And with the continued and significant increase in computing power for a fixed cost, even problems thought once to be intractable are now routinely solved with high-performance computing architectures or even desktop/laptop computing. The role of improved processor performance is unquestioned in helping to revolutionize the impact of computational science. However, equally as important are the algorithmic developments over the past few decades that have exploited any mathematical structure in the equations of interest to its full advantage. As an example, one needs only to consider adaptive time-stepping algorithms that are applied to the solutions of differential and partial

differential equations. Such algorithms aim to take as large a time-step as possible while being constrained to some absolute or relative error measure. So prevalent are these adaptive time-steppers that they are the standard, and expected, routines in most high-level language packages such as MATLAB, Octave or Scipy. In a similar fashion, we propose an *adaptive* time-stepping scheme where the *dimensionality* of the underlying system is adapted in order to more efficiently solve a given differential or partial differential equation system. Although dimensionality reduction techniques are well known, the method advocated here provides a hitherto unconsidered natural framework for a fully adaptive, robust and general time-stepping scheme which exploits optimal proper orthogonal decomposition (POD) basis modes whenever possible.

Dimensionality-reduction techniques, although around for more than a century [74–77], have recently grown in importance for solving a wide range of physical problems. The rise of such techniques often is related to the numerical discretization of PDE systems, for instance, that can often yield a system of equations with millions or billions of degrees of freedom (or more). Thus dimensionality reduction methods can form the underpinnings of developing reduced-order models through projections such as the proper orthogonal decomposition [74–80], which is, with potentially slight modification, also known as the Hoteling transform, Karhunen-Loéve expansion, principal component analysis (PCA), and/or empirical orthogonal functions (EOFs). Alternatively, it can be used in a slightly different manner in certain multi-grid methods, or for matrix approximation techniques, where the course-graining techniques first rely on some dimensionally reduced version of the problem one ultimately wishes to solve (See, for instance, Refs. [81–86]). Typically, such course-graining solution techniques are aimed at solving a large linear system (or performing a matrix completion) using iterative methods were progressively better (refined) guesses are achieved from a dimensionally reduced (course) grid. Much like the adaptive time-stepping algorithms, implementation of such multi-grid solvers are critical in rendering high-dimensional systems tractable.

This chapter aims to bring together well-known dimensionality reduction and adaptive time-stepping schemes with the goal of producing an intuitively appealing and natural, perhaps even obvious, time-stepping algorithm for differential and partial differential equations

that takes advantage of any low-dimensional, slow-manifold dynamics that exists in the system. Thus an adaptive time-stepping algorithm is demonstrated where dimensionality reduction is exploited whenever possible. The basis of such a strategy is rooted in the vast literature on coherent structures (low-dimensionality) that are observed to be prevalent in, for instance, PDE systems across a broad range of the physical, biological and engineering sciences [87]. Indeed, some underlying low-dimensional and slow-manifold seems to be the rule rather than the exception in observations of the dynamics of complex systems.

Many other techniques have also been recently advocated with the aim of exploiting some form of dimensionality reduction. In Schaeffer et al [88], *sparsity* is exploited by enforcing a soft thresholding at every time step to the coefficients of the basis approximation. By reducing or compressing the information needed to represent the solution at every step, only the essential dynamics are represented. Thus the basis modes are not modified, they are simply turned on and off as necessary at each time-step. Alternatively, one can capitalize on the newly developed dynamic mode decomposition (DMD) technique which projects onto a lower modal basis and evolves the future state according to a linear set of differential equations [89]. Although dimensionality reduction is achieved, the time-stepping equations are constrained to be linear. In yet another technique, a discrete empirical interpolation method (DEIM) [90] provides a modification of the POD method that reduces the complexity of evaluating the nonlinear terms of the reduced model to a cost proportional to the number of reduced variables obtained by POD. However, no adaptive stepping is considered. A version of *spatial* or *local* adaptivity for reduced order modeling has also recently been considered [91], but it enforces spatial dimensionality reduction rather than any adaptive time-stepping. And in a similar fashion, gappy POD has been considered as a means of using a small amount of data for efficient full state reconstruction [92,93]. Further algorithmic innovations have also been used to adaptively refine reduced-order models [94], potentially generate a set of internal variables to perform hyper-reduction of the complex system [95] and/or take larger time steps using online model reduction [96]. All the methods above have a clear goal: for a given accuracy, improve computational efficiency and significantly reduced computational time. The present technique advocated transforms to the guaranteed optimal basis (in an L^2 sense) so that a thresholding does not have to be applied at

each time-step (unlike Ref. [88]). Further, nonlinear evolution is allowed and adaptivity is central to the scheme unlike Refs. [89] and [90] respectively. Thus the method is demonstrated to be a highly successful, stand-alone algorithm which potentially could integrate some of the other techniques [88–90] to even greater effect.

More broadly, the algorithm advocated is an effective technique for automatic (adaptive) coarse graining of variables in complex systems. The underlying method uses POD to identify, in an online fashion, a reduced order model for the dynamics on the slow or inertial manifold. Such a coarse graining approach meshes well with a variety of burgeoning computational techniques for complex systems such as, for example, the equation-free (EF) method [97], the heterogeneous multi-scale method [98], the computational singular perturbation (CSP) method [99], and nonlinear Galerkin projection techniques [100]. What we demonstrate is an approach that is effective in solving difficult, high-dimensional problems that are important in a variety of fields. To some extent, the method can be thought of as a blend of EF methodology, since we are using *microscopic* PDE simulations to approximate the slow manifold, and nonlinear Galerkin or CSP methods since we time-step in a fashion which is a bit more complex than coarse projective integration. As with any dimensionally reduced basis, provided no *non-normal* modes are present to limit the validity of the POD approximations [101], the method is quite effective.

The chapter is outlined as follows. In the next section, the proper orthogonal decomposition with Galerkin projection is outlined as it applies to complex systems (in this case PDEs). Section 3 outlines the algorithm that takes advantage of the low-dimensional projections found in Sec. 2. In particular, the methods used to go from high-to-low and low-to-high dimensions are advocated. Section 4 demonstrates the successful application of the adaptive dimensionality time-stepper with three example PDEs. This is followed in Secs. 5 with an analysis of the computation time and error associated with implementing the time-stepping scheme. The chapter is concluded in Sec. 6 with an overview and outlook for the proposed time-stepping scheme.

6.3 Proper Orthogonal Decomposition and Galerkin Projection

Complex systems, which are often governed by nonlinear partial differential equations and/or large systems of differential equations, are typically beyond the reach of analytic methods and techniques for informing one of the underlying system dynamics. Computational methods, which yield high-dimensional systems, are thus employed to explore the behavior of the system in time and space as a function of the system parameters. But as is often the case, many high-dimensional systems elicit low-dimensional dynamical behaviors [87] that can be better understood using dimensionality-reduction methods [74–80].

One of the most important dimension reduction techniques is the proper orthogonal decomposition (POD) [79] that is based upon the singular value decomposition [102]. It reduces the dimension of the system of interest by projecting the full system onto the optimal (in an L^2 sense [102]) set of basis functions determined from empirical and/or computational data. The basic idea of the POD method is as follows: given a set of data that lies in space of dimension n, find a subspace of fixed dimension r, where $r \ll n$, such that the error in the projection onto the subspace is minimized.

For our purposes, and to illustrate the concept, consider a given PDE of the form

$$\frac{\partial A}{\partial t} = N\left(x, t, \frac{\partial A}{\partial x}, \frac{\partial^2 A}{\partial x^2}, ...\right) \tag{6.1}$$

where $N(\cdot)$ is in general a non-constant coefficient, time-dependent, and nonlinear function of $A(x,t)$ and its derivatives. Associated with Eq. (6.1) are also a set of boundary conditions in x and an initial condition $A(x,0)$. Solutions to Eq. (6.1) can be computed numerically by discretizing $A(x,t)$ into a series of spatial locations at time $t = t_j$ so that $A(x,t_j) \rightarrow \mathbf{a}_j$ where $\mathbf{a}_j = [a(x_1,t_j)\ a(x_2,t_j)\ \cdots\ a(x_n,t_j)]$. The discretized solution can then be advanced in time using standard methods including spectral, finite-difference, or finite element techniques, whichever is most appropriate for the given boundary conditions and geometry. In numerically solving Eq. (6.1), solution trajectories of the n-dimensional system in time are achieved. Our objective is to then arrange the numerical solution in a data matrix that includes m snapshots of the system:

$$\mathbf{X} = \Big[\mathbf{a}_1, \ldots, \mathbf{a}_m\Big] \tag{6.2}$$

where $\mathbf{a}_j$ with $j = 1, 2, \cdots, m$ determines the sampling of the solution at the prescribed times t_j.

Application of the singular value decomposition(SVD) to the data matrix $\mathbf{A}$ is guaranteed to yield the matrix decomposition

$$\mathbf{X} = \mathbf{U}\mathbf{\Sigma}\mathbf{V}^* = \Big[\phi_1, \ldots, \phi_n\Big] \begin{bmatrix} \sigma_1 & & & \\ & \ddots & & \mathbf{0} \\ & & \sigma_n & \end{bmatrix} \begin{bmatrix} v_{1,1} & \cdots & v_{1,m} \\ & \vdots & \\ v_{m,1} & \cdots & v_{m,m} \end{bmatrix} \tag{6.3}$$

where the diagonal matrix $\mathbf{\Sigma} \in \mathbb{R}^{n\times m}$ can be used to determine the rank (or approximate rank) of the data matrix and the matrices $\mathbf{U} \in \mathbb{C}^{n\times n}$ and $\mathbf{V} \in \mathbb{C}^{m\times m}$ contain the temporal and spatial projections of the data respectively.

The column vectors of $\mathbf{U}$, denoted by $\{\phi_j\}_{j=1}^n$, are called the POD basis modes. They are arranged in order of *importance* in an L^2 (energy) sense. Thus the first mode ϕ_1 accounts for the most "energy" in the data set $\mathbf{X}$, the second mode ϕ_2 contains the next most "energy" content and so forth. Moreover, all the modes are orthogonal so that their inner product satisfies the relation

$$\langle \phi_i, \phi_j \rangle = \int \phi_i \phi_j^* dx = \delta_{ij} \tag{6.4}$$

where δ_{ij} is the Dirac delta function and the integration is performed over the entire x range of the data set $\mathbf{X}$.

The critical observation of dimensionality reduction involves the so-called singular (diagonal) matrix $\mathbf{\Sigma}$. It is this matrix that will determine the nature of the low-rank subspace used in representing the dynamics contained in $\mathbf{X}$. The energy of each mode is defined as

$$E_j = \frac{\sigma_j^2}{\sum_{i=1}^n \sigma_i^2} \in [0, 1]\,. \tag{6.5}$$

By knowing the energy in each mode, and knowing they are ordered in importance from $j = 1$ (most dominant) to $j = n$ (least dominant), we can arbitrarily truncate the full n dimensional space to a low-rank subspace of dimension r where $r \ll n$. A guarantee of the POD basis is that they represent the optimal truncation in an L^2 sense. For instance, one may decide to work with a low-rank modal approximation that captures 99.9% of the

energy, i.e. $\sum_{j=1}^{r} E_j < 0.999$. Thus the rank r is determined by the arbitrarily imposed energy constraint.

So far, we have computed the POD basis of the solution given from the data matrix $\mathbf{X}$. We can then construct reduced order models using Galerkin projection on to the low-dimensional subspace using the truncated POD basis. We apply a Galerkin projection by simply projecting the original vector field $N(\cdot)$ in Eq. (6.1) onto the desired r-dimensional subspace spanned by $\{\phi_j\}_{j=1}^{r}$:

$$A_r(x,t) = \sum_{j=1}^{r} b_j(t)\phi_j(x)\,. \tag{6.6}$$

Substituting this approximation in to the governing equation (6.1), multiplying by ϕ_k^* and applying orthonormality generates the low-rank dynamic approximation

$$\dot{b}_k = \langle \phi_k, N\left(x, t, \frac{\partial A_r}{\partial x}, \frac{\partial^2 A_r}{\partial x^2}, ...\right)\rangle \tag{6.7}$$

for $k = 1, ..., r$. This resulting set of ODEs describes the evolution of the low-rank subspace spanned by $A_r(x,t)$. Provided $r \ll n$, the reduced system is of a much lower dimension while still capturing the dynamics of the full PDE system. Thus simulating the future state of the system is much more efficient in this basis decomposition since there are r ODEs instead of n ODEs to simulate. The error of the time-stepping will undoubtedly by determined by the truncation applied in determining the rank r of the subspace used. Recent results on using the DEIMs method [90] can potentially reduce the computation of the nonlinear terms and provide further computational savings. It should also be noted that constraining the solution to the above low-rank approximation proves difficult to rigorously justify, with only a few analytic results achieved to date [103]. Indeed, rigorous error estimates using dimensionality reduction techniques are an area of ongoing and active research given its wide-spread application in almost all branches of science.

This methodology, which we emphasize is fairly standard and well-known, has been applied successfully for representing the time-evolution of complex systems [78–80]. However, there is a clear disadvantage to this technique. Namely, once the low-rank basis modes $\{\phi_j\}_{j=1}^{r}$ have been selected, they are fixed and are incapable of representing "new" dynamics in the system, i.e. the modal basis set can only represent dynamics that are captured

in the data matrix $\mathbf{X}$. So if there is a bifurcation parameter in the system, or perhaps simply coefficients/parameters that evolve on slow time scales, the POD basis selected will generically be unable to accurately predict the future state of the system. In our method, this problem is circumvented by evaluating wether or not a new low-rank approximation is needed to represent the dynamics. Thus we do not fix a modal basis, but rather adapt the basis in time as required by the data matrix and subsequent sampling of the dynamics. The novelty of this chapter is in developing a technique and algorithm for adapting the modal basis in order to provide highly-efficient computations of complex systems.

6.4 Adaptive Rank-Selection Algorithm

The adaptive dimensionality stepping algorithm begins by considering the given partial differential equation (6.1) that is discretized on a specified domain into an n-dimensional system. The first step of the adaptive algorithm is to time-step the full, n-dimensional PDE system for a prescribed time to obtain the solution data matrix $\mathbf{X}$ which samples the solution over a prescribed time Δt. Due to the fact that the POD approach doesn't rely on any prior knowledge of the process that generates the data, any appropriate numerical method can be applied to the full PDE simulation, for instance, a spectral method or finite difference scheme. As soon as enough simulation data has been obtained to construct the data matrix $\mathbf{X}$, a check is made to see whether or not it is possible to switch to a low dimensional POD basis and solver. Typically this happens if the simulation has evolved onto the low-dimensional (slow) manifold of the governing equations. If no reduction is possible, then the full n-dimensional time-stepping algorithm continues to advance the solution in time.

We will introduce *three* approaches for testing for a potential reduction from the full n-dimensional discretization to an r-dimensional POD approximation where $r \ll n$. If the decision made by the algorithm is to switch to a low dimensional POD evolution, it will compute the POD basis using a standard SVD decomposition. The initial condition used for the POD expansion is computed using the projection of the last snapshot of the data matrix $\mathbf{X}$ onto the POD basis. The time-stepping algorithm will then advance the solution in the low-rank subspace of dimension r. Typically, this is the approach advocated when implementing the POD bases [78–80]. However, for the time-stepping advocated

here, it is critical to check when the POD basis fails to properly encode, or represent, the dynamics of the full system n-dimensional system. Thus it is also important to determine when to go from the low-rank system back to the full-rank system in the simulation. In what follows, *two* approaches are demonstrated which systematically check for the required *dimensionality-inflation* procedure. Thus if a dimensionality-inflation is required, then the time-stepping algorithm in the r-dimensional POD basis is recast back into the full n-dimensional computational framework. Figure 6.1 shows a flowchart of the adaptive POD algorithm described above. By judiciously using dimensionality-reduction (rank r) and -inflation (rank n), an efficient time-stepping algorithm is demonstrated that optimally takes advantage of the low-dimensional behavior in the system whenever it is possible to do so.

6.4.1 Dimensionality reduction: from rank n (high) to rank r (low)

The following subsections propose three different dimensionality reduction techniques capable of providing robust low-rank approximations to the governing equations. They are presented in order of increasing computational complexity: from simple $O(N)$ checks to full $O(N^3)$, SVD based methods. Of course, one would use the simple scheme when possible and resort to the SVD-based check only when necessary. The checking represents an overall computational *overhead* for evaluating the future state of the system.

Test 1: Steady-State L^2-Norm Test

The first test for dimensionality reduction is a low-cost method based upon an L^2 norm test of the solution. This approach works especially well for detecting steady state solutions. Assume $A(x,t)$ is the solution of the full PDE (6.1) in the subinterval $t \in [t_n, t_n + \Delta t]$ for some prescribed Δt which is not the time-integration time-step (generally $\Delta t \gg \delta t$ where δt is the numerical time-step). If it is a steady state solution, then a simple check for low-rank behavior can be obtained by considering the quantity:

$$e_n = \frac{\|A(x, t_n + \frac{\Delta t}{2}) - A(x, t_n + \Delta t)\|}{\|A(x, t_n + \Delta t)\|} < \epsilon \tag{6.8}$$

for the given Δt. For very small ϵ, in the range of numerical roundoff, this property suggests a switch to the r-dimensional low-rank POD solver without any trouble since a low-rank

subspace (steady-state) solution has been reached.

Test 2: Center-of-Mass Test

Although the L^2-Norm Test works perfectly well for stationary solutions, it fails to identify low-rank, time-dependent solutions such as, for instance, breathers. Breather solutions are low dimensional, thus a low dimensional POD solver can be applied. However, many time-dependent, perhaps chaotic, solutions are not low-rank and the low-dimensional POD solver is a poor choice for representing the solution. Thus it is important to differentiate between low-rank breather-type solutions and more exotic, and not low-rank, time-dependent solutions in the adaptive time-stepping method. To do this, we introduce $\bar{x}$ which is the center-of-mass defined as

$$\bar{x}(t) = \frac{\int xA(x,t)dx}{\int A(x,t)dx}\,. \tag{6.9}$$

For symmetric breather solutions, the value of $\bar{x}(t)$ is constant. Of course, just like Test 1, the center-of-mass test fails to capture low-rank solutions with symmetry or invariance properties such as rotation or translation. However, the test can be modified and/or redesigned for this as well [80, 106].

For multi-pulse stationary solutions considered here, for instance, the center of mass $\bar{x}(t)$ is also a constant. So in each subinterval, we can check whether the dynamics is low dimensional by evaluating the center-of-mass function $\bar{x}(t)$. Assume we are working on subinterval $t \in [t_n, t_n + \Delta t]$ for a prescribed Δt as before. The time shift indicator $\bar{x}_{shift}$ is defined in the following form:

$$\bar{x}_{shift} = \frac{1}{\Delta t}\int_{t_n}^{t_n+\Delta t} |\bar{x}(t) - \bar{x}(t_n + \Delta t)|dt\,. \tag{6.10}$$

If $\bar{x}_{shift}$ is greater than a given threshold value ϵ, we can be confident that in the current subinterval, it is not a simple steady-state of time-periodic solution. However, if $\bar{x}_{shift}$ is less than the prescribed threshold value of ϵ, a low rank POD solver can be applied to obtain a more efficient computation of the solution in time. Like the first test, this is a more computationally efficient test than a full SVD reduction.

Test 3: Number of SVD Modes Test

An SVD decomposition is the most robust, and costliest test, available for evaluating the rank of the data matrix. Thus in addition to the two previous tests, both of which are numerically efficient to evaluate, we can SVD a given number of snapshots of the data in the time interval $t \in [t_n, t_n + \Delta t]$. For this case, the SVD requires an $O(N^3)$ operation where N is the size of the data matrix $\mathbf{X}$. For this case, we evaluate the number of modes required to represent a certain amount of energy in the data matrix $\mathbf{X}$, say 99.999% of total energy. For steady state and breather solutions, this number is indeed extremely small, often one and 2-3 modes respectively. For more exotic solutions, more modes may be required, but as long as they are of much smaller rank than the dimension of the original data matrix, computational savings can be established. Utilizing the above strategy, the number-of-modes test can be used to classify the current low-rank nature of the dynamics of the equation, ultimately leading to a switching from full PDE simulations to a low dimensional POD solver.

In practice then, a simulation of the full PDE is performed over a given subinterval $t \in [t_n, t_n + \Delta t]$ to generate the data matrix $\mathbf{X}$. Applying the SVD to this matrix yields the singular matrix which allows for an evaluation of the low-rank nature of the data. If the SVD shows the solution to be of sufficiently low-rank, as determined by the user, the POD modal basis $\{\phi_j\}_{j=1}^{r}$ is chosen and the Galerkin projection (6.6) is used to time-step forward into the future. This basis is used until it no longer is able to capture the correct dynamics of the full PDE system.

6.4.2 Dimensionality Inflation: from rank r (low) back to rank n (high)

This subsection is concerned with determining when the POD approximation breaks down. In particular, it is fairly easy to understand when the solution has become low-rank, and the previous section describes three techniques for doing so. However, once you have recast the problem in the low-rank space, it is imperative to determine when one has to once again return to the full, high-dimensional PDE computation. Two robust techniques are highlighted here.

Test 1: Auxiliary Modes Test

Assuming the first r modes $\{\phi_j\}_{j=1}^{r}$ from the full, high-dimensional PDE simulations contain a prescribed amount of energy required to approximate the system with some precision, we can add m extra modes to the truncated POD basis and project the solution onto the combined $r+m$ modes. This is called the extended basis. From our numerical experiments, we know that the m auxiliary modes should only contain negligible amounts of energy beyond the truncation at r modes. Thus we can use the energy content in these m auxiliary modes as a probe which can tell us if the low rank POD solver works well for the current subinterval, or if it needs to be replaced by full PDE simulation. More precisely, since the energy on the extra m modes are quite low (usually less than 10^{-10} in our applications), adding them to the rank r truncated POD basis $\{\phi_j\}_j = 1^r$ should not affect the accuracy of the solver. However, when the extended POD basis fails to capture the dynamics of the system, the energy of these m auxiliary modes will grow significantly. Thus a reliable test for checking for the necessity of switching to full PDE simulation is provided by monitoring the energy on these m modes. Since it is not possible to track the energy as defined in Eq. (6.5), we use instead the proxy energy metric:

$$\mathcal{E}_j = \frac{b_j^2}{\sum_{i=1}^{r+m} b_i^2} \in [0,1] \tag{6.11}$$

where the b_j are the POD coefficients obtained by Galerkin projection defined in Eq (6.6). Essentially, this definition of energy is equivalent to Eq. (6.5). However, it can be easily computed in our low dimensional POD solver. With this solver, the energy in the m auxiliary modes can be easily evaluated. It is observed that when the energy in the auxiliary modes grow, then the rank r POD projection no longer accurately captures the full PDE dynamics and dimensionality inflation must be performed.

Test 2: Residual test

In addition to the auxiliary mode test, which is fairly simple and computationally efficient to perform, there is a second obvious test for evaluating the appropriateness of the low-rank POD approximation. This test, called the residual test, simple checks the to see if the POD

expansion satisfies the governing equations to some prescribed accuracy. Specifically, the PDE satisfies (6.1). The residual of the PDE is defined as

$$R = \frac{\partial A_r}{\partial t} - N\left(x, t, \frac{\partial A_r}{\partial x}, \frac{\partial^2 A_r}{\partial x^2}, ...\right) \tag{6.12}$$

where A_r is the low-rank POD solution. Although the residual is not equivalent to the error, it is a proxy for it. Thus intuitively, if the residual is greater than a specified tolerance, then the numerical algorithm is considered to have failed in representing the PDE solution. In contrast, if the residual remains bounded below some prescribed tolerance level, then the low-rank POD projection is considered to be a successful representation of the full solution. This second dimensionality inflation test is more computationally costly than the auxiliary mode test, but it does provide a more concise measure of the error in approximating the solution.

6.5 Applications

To test the dimensionality reduction and inflation techniques advocated in the previous section in an adaptive dimensionality numerical scheme, three example PDE systems will be considered. Not only will a direct comparison be made between the full PDE and low-rank POD projection, but an evaluation of the computational efficiency will be provided. The methods advocated for going from high-to-low (reduction) and low-to-high (inflation) dimensions are shown to be quite effective, thus supporting the idea of adaptive time-stepping schemes based upon dimensionality.

6.5.1 Model 1: cubic-quintic Ginzburg-Landau equation

One of the prototype models of mathematical physics is the cubic-quintic complex Ginzburg-Landau equation (CQGLE). As discussed in section 2.2, here CQGLE model is considered in context of mode-locked laser theory and periodic boundary conditions are assumed in the computational scheme with a given non-zero (white-noise) initial condition.

In our numerical experiment, the parameters are taken to be the following: $D = 0.4$, $\gamma = 1$, $\nu = 0.01$, $\tau = 0.1$, $\delta = 1$, $\beta = 0.3$, $\mu = 0.02$ and $e_0 = 1$. Our bifurcation parameter is the gain parameter g_0. Specifically, when the value of gain g_0 is increased, the stable pulse

solution undergoes a multi-pulsing transition which is commonly observed in mode-locking system [66]. This property allows us to test whether the adaptive POD algorithm can capture the dynamics of PDEs when the parameter is changed and corresponding change of dynamics occurs.

In our prototypical numerical experiment, we let g_0 be a step function which is defined as follows

$$g_0(z) = \begin{cases} 2.0 & : z \in [0, 1250) \\ 5.5 & : z \in [1250, 2500) \\ 0.8 & : z \in [2500, 3750) \\ 3.24 & : z \in [3750, 5000] \end{cases} \tag{6.13}$$

In the initial time interval with $g_0 = 2$ a one-pulse solution quickly forms. When g_0 is increased to 5.5, the solution bifurcates to a three-pulse solution. When g_0 is decreased to 0.8, the one-pulse solution reforms (different than the original one-pulse). Finally, a two-pulse solution is formed when we increase the gain value g_0 to 3.24. The full PDE solution, which represents the *truth*, is performed using a Fast Fourier Transform discretization in the spatial domain in combination with a standard 4th-order Runge-Kutta time-stepping scheme in time.

In implementing the adaptive POD algorithm, the low-dimensional (rank r) Galerkin truncation for (2.2) must be computed. Following (6.4)-(6.7) leads to the low-rank system:

$$\begin{aligned} \frac{db_k}{dz} = \left(\frac{iD}{2} + g(z)\tau\right) \langle \sum_{j=1}^{r} b_j \phi_j'', \phi_k \rangle + (\beta + i\gamma) \langle | \sum_{j=1}^{r} b_j \phi_j |^2 \sum_{j=1}^{r} b_j \phi_j, \phi_k \rangle \\ -(\mu + i\nu) \langle | \sum_{j=1}^{r} b_j \phi_j |^4 \sum_{j=1}^{r} b_j \phi_j, \phi_k \rangle \\ +(g(z) - \delta) \langle \sum_{j=1}^{r} b_j \phi_j, \phi_k \rangle \qquad k = 1...r \end{aligned} \tag{6.14}$$

This prescribes the equations of motion once a dimensionality reduction test has been performed and a low-rank approximation has been determined to be suitable. The flowchart in Fig. 6.1 outlines the algorithm that is now implemented for solving (2.2). Figure 6.2 shows the effectiveness of the adaptive POD solution to the CQGLE with the time-dependent g_0 values given by (6.13). The red regions denote where the full PDE system is implemented

while the blue regions are the dimensionality reduced areas. The dominance of the blue regions ensures a significant computational savings.

6.5.2 Model 2: Waveguide Array Mode-Locking

A second example model considered is that of a system of coupled partial differential equations. As discussed in section 2.3, much like the CQGLE example, the application context of waveguide array mode-locking is in the arena of optical mode-locking. In our numerical experiment the parameters above are chosen to be: $D = 1$, $\beta = 8$, $C = 5$, $\gamma_0 = 0$, $\gamma_1 = 0$, $\gamma_2 = 10$, $\tau = 0.1$, $e_0 = 1$. The gain parameter g_0 is allowed to be varied and is the bifurcation parameter in the experiment. Single-pulse mode locking, breathers, chaotic and multi-pulse solutions can all be obtained as the value of g_0 is varied [104, 105]. In order to test whether the adaptive method is able to handle the transition between different types of dynamics, we let g_0 to be the step function:

$$g_0(z) = \begin{cases} 3.5 & : z \in [0, 1000) \\ 0.6 & : z \in [1000, 1500) \\ 2.3 & : z \in [1500, 2000) \\ 4.3 & : z \in [2000, 5000] \end{cases} \tag{6.15}$$

For these parameters, the dynamics first exhibits a stable two pulse mode-locking scenario. Upon decreasing the gain to $g_0 = 0.6$, a low amplitude one-pulse solution if formed. Raising the gain to $g_0 = 2.3$ produces a high-amplitude one-pulse mode locking solution that bifurcates to a three-pulse solution immediately after g_0 is increased to 4.3. By Applying the adaptive POD algorithm to WGAML, we generate the same dynamics as that observed in the full PDE simulation (See Figure 6.3).

6.5.3 Model 3: Two-dimensional cubic-quintic Ginzburg-Landau equation

As a final example, we consider the two-dimensional CQGLE (2D-CQGLE) discussed in section 2.4, which is proposed to model cavity soliton formation [107]. In the numerical experiments that follow, the equation parameters are set to the following: $D = 0.5$, $\gamma = 1.5$, $\nu = 0.08$, $e_0 = 1$, $\tau = 0.1$, $\delta = 1$, $\beta = 0.8$ and $\mu = 0.5$. The time dependent bifurcation

parameter g_0 is chosen to be the following step function:

$$g_0(t) = \begin{cases} 1.45 & : z \in [0, 1250) \\ 3.6 & : z \in [1250, 3000) \end{cases} \tag{6.16}$$

The increase in the gain assures that the solution bifurcates from a single localized cavity soliton to two localized cavity solitons in the transverse field.

The adaptive POD time-stepper applied to the 2D-CQGLE yields the same results as the full PDE simulations of (2.6). Figure 6.4 shows a topographical view of the dynamics at different time points as the system undergoes a dynamical state change. Additionally, the bottom panel demonstrates when the system solves the full PDE system (shaded region) versus using a dimensionally reduced bases. The adaptive solver switches between the full PDE solver and the low dimensional solver automatically when appropriate, i.e, in the transition region between the one-pulse and two-pulse region. The dimensionality reduction in this case is exceptionally efficient for solving the governing 2D-CQGLE as the 2D discretization yields an $O(N^2)$ system of ODEs unlike the $O(N)$ system in one dimension.

6.6 Computation Efficiency and Error Analysis

Two standard criteria are used to evaluate the adaptive dimensionality time-stepping scheme: the computational efficiency and its accuracy. Since the truncated POD basis approximates well the full PDE solution with only a few modes, the potential for computational improvement is significant since the time-stepping can now be performed with only a few modes of an ODE solver. In what follows, an assessment will be made of the computational time and error of the scheme when applied to the three given examples of the last section.

6.6.1 Computational Time

Since the adaptive dimensionality time-stepping algorithm switches between the full PDE simulation and the low dimensional POD solver automatically, the complexity of the algorithm is difficult to evaluate directly. However, the complexity of the low dimensional POD solver can be studied in order to evaluate the potential computational savings.

In this evaluation, the CQGLE (model 1) is chosen as the test problem. The model is

Table 6.1: CQGLE CPU time

method	CPU time
FFT	$2.5282e+3$
POD 1mode	24.5563
POD 2modes	64.9333
POD 3modes	118.5226
POD 8modes	157.6589
POD 16modes	280.6967
POD 32modes	$4.7241e+3$
POD 64modes	$1.4457e+4$
POD 128modes	$4.3655e+4$

solved as previously using a PDE simulation based upon spectral techniques (Fast Fourier Transform) in interval propagation interval $Z \in [0, 50]$ for a fixed g_0 supporting a single pulse. The spatial domain $T \in [-20, 20]$ is discretized into $n = 512$ Fourier modes with an initial condition $u(0, t) = sech(t)$. After the sample (or truth) solution in the interval $Z \in [0, 50]$ is obtained, the POD algorithm is applied to solve the equation for the propagation interval $Z \in [50, 2000]$. The computation time of the POD solutions are then compared with that of solution computed by full PDE simulation and the results are showed in the Table 6.1. The table shows that if 16 modes are kept in the POD algorithm, it only cost 10% of the computation time compared with full PDE simulation. As the modes are increased, the POD algorithm can become more costly as there is the extra cost of computing inner products of the POD modes etc. However, 16 modes are shown to be more than enough modes to ensure that the dominant error arises from the Runge-Kutta stepper itself (error of 10^{-6}). In fact, in most cases, by keeping only 8 modes in the POD solver, an accuracy of 10^{-7} can be achieved. Thus the 512 modes are swapped out for an 8 mode representation. This represents a significant, order-or-magnitude computational savings.

We further considered the adaptive POD algorithm applied to all three models presented

Table 6.2: CPU Time: Adaptive POD vs FFT

	CQGLE	WGAML	2D-CQGLE
FFT	$1.2786e+4$	$1.5407e+4$	$1.6347e+5$
Adaptive POD	$1.0864e+3$	$5.2564e+3$	$7.0931e+4$

Table 6.3: Computation Time distribution

	CQGLE	WGAML	2D-CQGLE
FFT	892.0613	$4.0525e+3$	$6.5742e+4$
POD	194.0739	$1.2031e+3$	$5.1846e+3$
Test	0.0107	0.3305	1.3216
SVD	0.3298	0.4931	3.1109

in the previous section: the CQGLE, WGAML and 2D-CQGLE. The computation times of the adaptive method was compared with that of full PDE simulations. For CQGLE, the propagation interval was $Z \in [0, 5000]$ (using $\Delta Z = 0.2$) with spatial domain $T \in [-20, 20]$ and $n = 1024$ Fourier modes and initial conditions $u(0,t) = sech(t)$. For the WGAML model, the propagation interval was $Z \in [0, 4000]$ with spatial domain $T \in [-10, 10]$ and $n = 512$ Fourier modes with initial conditions $A_0(0,t) = sech(t)$, $A_1(0,t) = 0$ and $A_2(0,t) = 0$. For the 2D-CQGLE, the time interval $t \in [0, 9000]$ with transverse domain $[x, y] \in [-20, 20] \times [-20, 20]$ with $n = 512$ Fourier mode discretization in each direction and initial conditions $u(0, x, y) = \exp(-x^2/4 - y^2/4)/2$. A computation time comparison using dimensionality reduction for these three prototype models is shown in Table 6.2. As is evident, the adaptive POD solver significantly reduces the computation time, typically by an order of magnitude for the same accuracy. In addition, we also tracked the computation time required of each part of the adaptive POD method, which is listed in Table 6.3. The SVD decomposition and switching test only takes a very small amount of time suggesting that the algorithm is efficient.

Table 6.4: Convergence of low dimensional POD solver

Tol	1mode	2 modes	3 modes	8 modes	16 modes	32 modes	64 modes
10^{-5}	2.7×10^{-3}	2.7×10^{-3}	3.7×10^{-7}	1.4×10^{-7}	1.4×10^{-7}	1.4×10^{-7}	1.4×10^{-7}
10^{-16}	2.7×10^{-3}	6.4×10^{-6}	3.7×10^{-7}	1.2×10^{-7}	1.3×10^{-7}	2.7×10^{-7}	3.9×10^{-7}

6.6.2 Error Analysis

To assess the error of the adaptive dimensionality time-stepping algorithm, simulations are compared directly to highly resolved PDE simulations. To demonstrate this in concrete terms, the solution of the CQGLE is sampled in the interval $Z \in [0, 50]$ and the SVD is applied to the sample solution to generate the POD modes. A 1, 2, 3, 8, 16, 32 and 64 POD mode reduction is considered. The relative error of these reductions is defined as

$$e = \frac{\| |u_{POD}| - |u_{FFT}| \|_\infty}{\|u_{FFT}\|_\infty} \tag{6.17}$$

The error for the dimensionality reductions are showed in Table 6.4. Note the rapid convergence of the low dimensional POD solver when the number of modes is increased.

6.7 Summary

Dimensionality reduction methods are becoming common place for analyzing and assessing the dynamics and evolution of complex systems arising in the engineering, biological and physical sciences. This is due, in large part, to the very high-dimensional nature of the complex systems when solved using computational discretization methods. And although algorithms are often readily available for time-stepping, the sheer size of the resulting discretization renders such computational solutions inefficient and extremely costly. Ultimately, such techniques highlight the need for data analysis methods applied to the underlying dynamical systems.

Our objective in this chapter is to consider efficient time-stepping algorithms and schemes for solving seemingly high-dimensional complex systems. The critical observation is that complex systems almost always exhibit dynamical evolutions that occur on low-dimensional

manifolds, thus suggesting that if this manifold can be found, the dynamics would then have a natural basis on which to evolve. Moreover, the high-dimensional simulation (of dimension n) that occurs on the discretized basis reduces to simulation on the low-dimensional manifold (or rank r). The computational savings are readily apparent since $r \ll n$. Much like adaptive time-stepping algorithms which take as large a step as possible while preserving a prescribed accuracy, we demonstrate that an adaptive dimensionality algorithm allows for a greatly improved efficiency in solving a number of example PDEs, often performing computations an order or magnitude quicker than their standard discretization counterpart.

Given the demonstrated success of the method, some outstanding issues still remain. In particular, the method is limited to complex systems that exhibit slow manifold dynamics that act as attractors to the system. If the dynamics does not have such underlying structure, then low-rank approximations generally do not hold. The method also fails during transient dynamical responses. Finally, if there are low-rank, slow manifolds that are subject to invariances such as translation or rotation, the method as shown here fails to capture the low rank structure. However, the algorithm can be easily modified to handle such invariances [106]

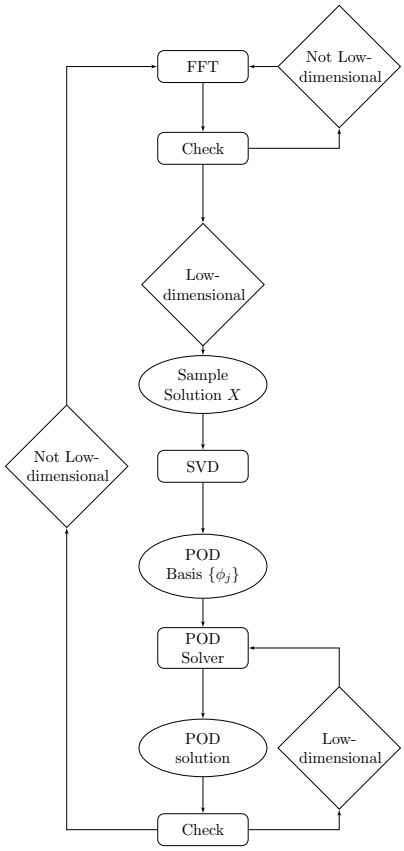

Figure 6.1: Example flowchart for implementing the adaptive POD algorithm. In this case, a spectral method using the fast Fourier transform is implemented so that the FFT represents the full simulation of rank n. The POD solver is implemented using an r-rank approximation where $r \ll n$.

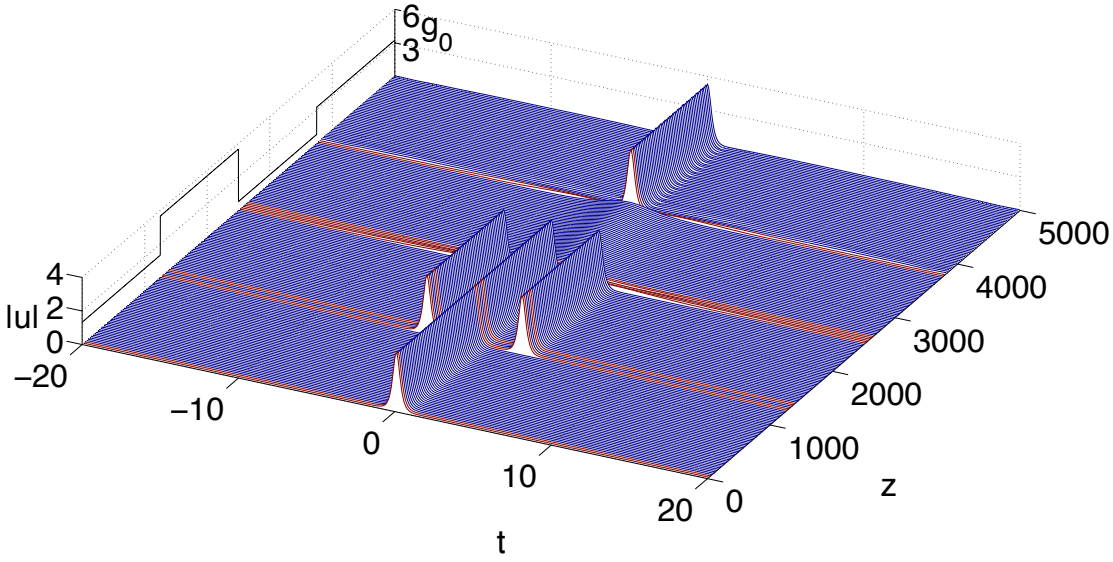

Figure 6.2: Waterfall plot of solution to the CQGLE obtained by the adaptive POD algorithm. The simulation matches the full PDE simulation as demonstrated in the error analysis of Sec. 6.6. The red region corresponds to the region where the full PDE solver is evoked by the algorithm while the blue region corresponds to where the low dimensional POD solver is chosen. The time-dependent bifurcation parameter g_0 is illustrated at left.

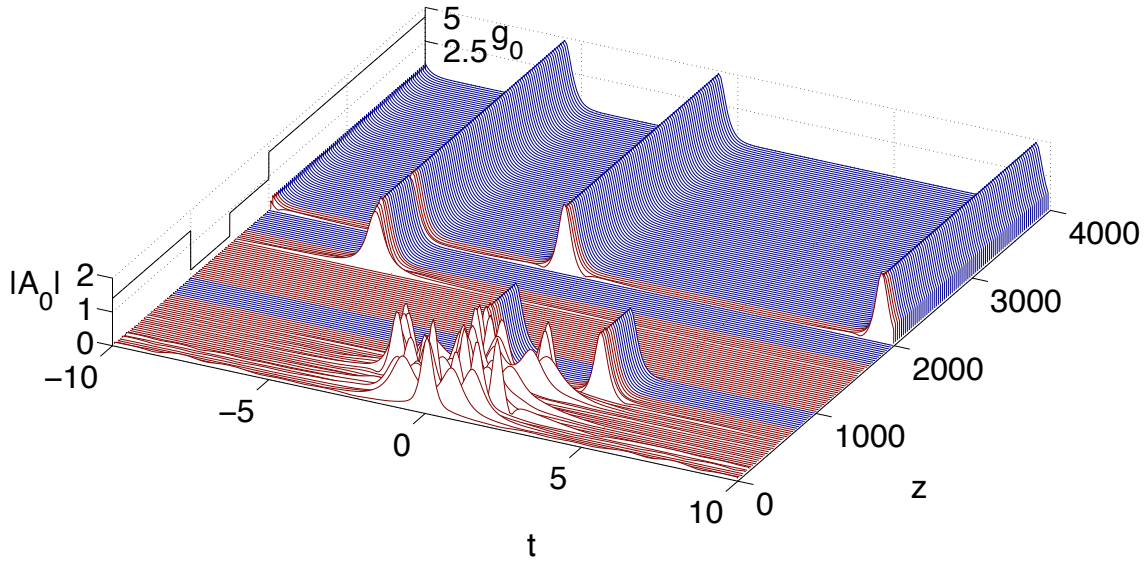

Figure 6.3: Waterfall plot of solution to the WGAML obtained by the adaptive POD algorithm. The simulation matches the full PDE simulation as demonstrated in the error analysis of Sec. 6.6. The red region corresponds to the region where the full PDE solver is evoked by the algorithm while the blue region corresponds to where the low dimensional POD solver is chosen. The time-dependent bifurcation parameter g_0 is illustrated at left.

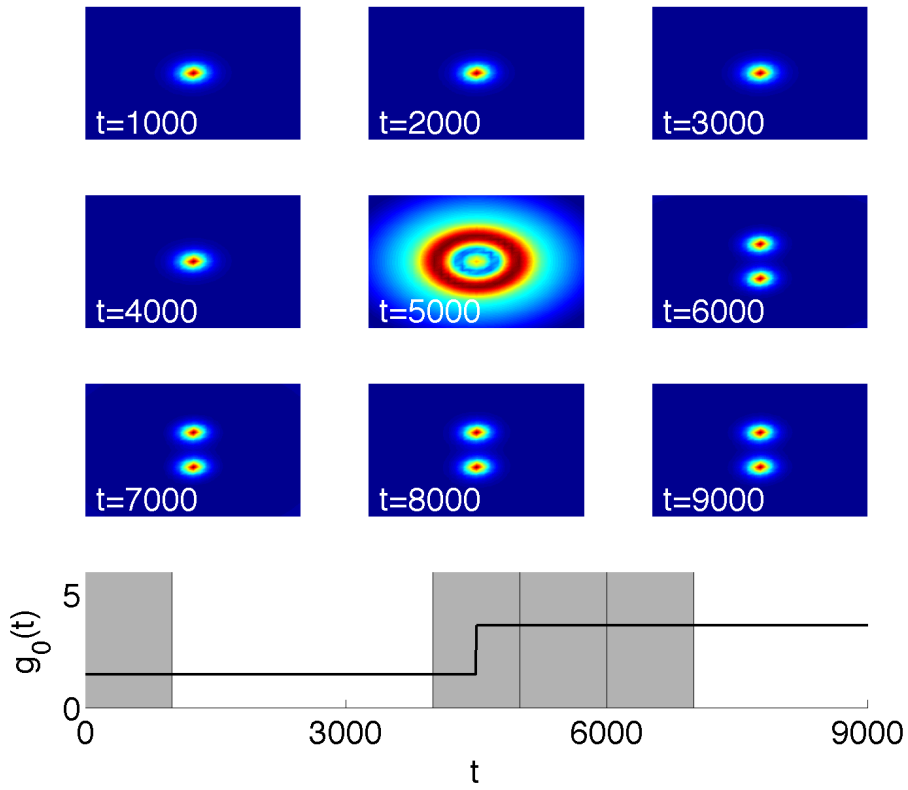

Figure 6.4: Dynamic evolution of the 2D-CQGLE obtained by using the adaptive POD algorithm. The solution matches the evolution of the full PDE solution (See Sec. 6.6). As the time dependent bifurcation parameter g_0 is increased, the solution dynamically evolves from a one cavity soliton to a two cavity soliton solution. The bottom panel indicates the changes in the bifurcation parameter as a function of time. In this bottom panel the shaded region corresponds to the region where the full PDE solver is evoked by the algorithm while the unshaded (white) region corresponds to where the low dimensional POD solver is chosen.

Chapter 7

CONCLUSIONS

In this thesis, various types of data-driven methods including genetic algorithm, extremum seeking, library building and sparse representation are successfully applied to mode-locked lasers.

In chapter 3, a multi-NPR mode-locked fiber laser with a genetic algorithm optimization is established which allows one to build a more stable, reliable, and most importantly, high-energy fiber laser system that can compete directly with their solid state counterparts. As a consequence of this work, a multi-NPR configuration with a multi-grid genetic algorithm control loop is established as a highly desirable design tool for engineering high-energy laser cavities. And as a final note, one can imagine replacing the NPR devices considered here, i.e. sets of waveplates and polarizer, with a much cheaper all-fiber based NOLM or NALM device. Indeed, given the prohibitively high cost of inserting additional NPRs (3 waveplates, one polarizer, and an additional amplifier), low-cost alternatives are critical to assessing the success of the multi-transmission curve engineering. Initial indications suggest that the additional amplifiers can be removed from the cavity while retaining close to the same performance gains observed here. Moreover, by replacing the three waveplates and polarizer with a NOLM, for instance, further reduction in cost can be achieved without sacrificing the projected performance gains. What is so compelling about the genetic algorithm implementation is that it simply does not care about the specific details of implementation. Rather, it measures the performance directly of the laser cavity and tunes the parameters it is allowed in order to achieve optimal performance. This is especially important when using a NOLM in the cavity as many of the leading theories for NOLMs are arrived at using simplifications that do not hold in practice, thus rendering the theoretical portion suspect in the optimization process. The genetic algorithm would make direct use of experiment versus theory in tailoring the NOLM settings for enhanced energy production. Such considerations

will be made in future work.

In chapter 4, we developed a extremum-seeking controller for the passively mode-locked fiber laser based on NPR. The controller simultaneously varies the waveplates and polarizer angles in a single-NPR laser to maintain a high-energy mode-locked state under large, rapid changes in the birefringence. The control architecture demonstrated in this chapter generalizes to multiple-NPR laser systems. However, these systems are extremely expensive to simulate because of the multiple time-scales, especially for a long, time-resolved signal, as in Figures 4.9. A next-step is to apply these methods in an experiment, and begin increasing the number of NPR sections, which will result in a higher energy pulse. Indeed, the extremum seeking control advocated here may be the only practical way to explore such high-dimensional parameter regimes. The methods in this chapter rely on a decent set of starting parameters, so that we are in the attracting basin of a local maximum. For multiple-NPR systems, this parameter space is high-dimensional, and new techniques will need to be developed to identify good starting guesses for the extremum-seeking controller. This may well involve the use of machine learning and data reduction techniques, as in [67]. The extremum-seeking controller may also be used to simply monitor and maintain robust operation of a mode-locked laser. For instance, it may be beneficial to turn on the extremum-seeking controller for a short time to search for the locally optimal parameter values and then fix the angles during operation for improved pulse uniformity. The objective function can be continually monitored, even without perturbing the input parameters, allowing for the construction of a switching criteria to turn on the extremum-seeking controller. Finally, given the success of the algorithm in the NPR laser, one can easily imagine applying the same techniques to other classes of both solid state and fiber lasers. As long as one can clearly identify parameters which manipulate the mode-locking, then these parameters can be controlled by the algorithm. Alternatively, one can use the algorithm with an objective function that seeks to recover other mode-locking states of interest, wether they be the fastest temporal pulses, pulses with prescribed spectral shapes, etc. Thus it is a general framework that can be easily integrated into practical photonics systems with the potential of great success.

In chapter 5, we showed that a toroidal search based library building and searching

algorithm for characterizing the birefringence change of a mode-locked laser cavity. A very high recognition rate is achieved for birefringence characterizing, thus suggesting the algorithm is highly promising for application purposes. Most importantly, although the algorithm was designed on an underlying theoretical model, due to its data-driven nature, the method can be integrated directly into an experimental laser cavity. Philosophically, the approach taken in this chapter does not attempt to construct a better model of birefringence and its stochastic fluctuations. Rather, the cavity birefringence simply is what it is, and the goal is to use state-of-the-art data methods for classifying the birefringence into a previously learned library, i.e. the library and classifier become the expert-in-the-loop. Once classified, the optimal waveplate and polarizer settings are then already known from the toroidal search algorithm. This ultimately leads to an efficient, self-tuning laser since the waveplates and polarizers can be adjusted directly to their optimal positions using servo-control motors [23,70]. Specifics of the physical implementation are given in Fig. 5.8 with the training and execution algorithms given by the pseudo-codes in Table 5.1. The flow charts and algorithm architecture, which are color coded with each other, illustrate the practical implementation of the method. More broadly, such difficulties in quantitative modeling are a hallmark feature of complex systems which display some underlying stochastic dynamics. For instance, the modeling of climate and weather is extremely difficult due to underlying stochastic, micro-scale physics. In such complex systems, data-driven modeling techniques are critical for improving quantitative predictions. In weather forecasting, for instance, data-assimilation methods have been critical in achieving better performance (accuracy) and longer forecast windows [80]. Thus instead of attempting to construct more refined, and typically over-parametrized models for the stochastic effects, the goal is to simply make use of recognized, coherent patterns of activity and direct measurements to inform decisions about the state of the system. The demonstration here shows that such a method is highly effective for modeling fiber lasers.

Moreover, in chapter 6, we discussed time-stepping algorithms and schemes for solving high-dimensional complex systems. One critical observation here is that complex systems almost always exhibit dynamics that sit on low-dimensional manifolds, thus suggesting that the dynamics should have a more natural basis on which to evolve. We demonstrate that

an adaptive dimensionality algorithm provides a big improvement in efficiency when used to solve example PDEs. Such computational savings should clearly be taken advantage of in any time-stepping scheme and we provide a number of robust example methods for performing the required dimensionality reduction and inflation associated with our proposed algorithm.

BIBLIOGRAPHY

[1] D. J. Richardson, J. Nilsson, and W. A. Clarkson, "High power fiber lasers: current status and future perspectives," J. Opt. Soc. Am. B **27**, B63-B92 (2010).

[2] H. A. Haus, "Mode-locking of lasers," IEEE J. Sel. Top. Quant. Elec. **6**, 1173-1185 (2000).

[3] K. Tamura, E.P. Ippen, H.A. Haus, and L.E. Nelson, "77-fs Pulse generation from a stretched-pulse mode-locked all-fiber ring laser," Opt. Lett. **18**, 1080-1082 (1993).

[4] K. Tamura and M. Nakazawa, "Optimizing power extraction in stretched pulse fiber ring lasers," App. Phys. Lett. **67**, 3691-3693 (1995).

[5] G. Lenz, K. Tamura, H. A. Haus, and E. P. Ippen, "All-solid-state femtosecond source at 1.55 μm," Opt. Lett. **20**, 1289-1291 (1995).

[6] F. Ö. Ilday, J. Buckley, and F. W. Wise, "Self-similar evolution of parabolic pulses in a laser cavity," Phys. Rev. Lett. **92**, 213902 (2004).

[7] W. H. Renninger, A. Chong, and F. W. Wise. "Self-similar pulse evolution in an all-normal-dispersion laser." Phys. Rev. A **82**, 021805 (2010).

[8] B. Bale and S. Wabnitz, "Strong spectral filtering for a mode-locked similariton fiber laser," Opt. Lett. **35**, 2466-2468 (2010).

[9] A. Chong, W. H. Renninger, and F. W. Wise, "Properties of normal-dispersion femtosecond fiber lasers," J. Opt. Soc. Am. B **25**, 140-148 (2008).

[10] S. Namiki, E. P. Ippen, H. A. Haus, and C. X. Yu, "Energy rate equations for mode-locked lasers," J. Opt. Soc. Am. B **14**, 2099-2111 (1997).

[11] B. G. Bale, K. Kieu, J. N. Kutz, and F. Wise, "Transition dynamics for multi-pulsing in mode-locked lasers," Opt. Express **17**, 23137-23146 (2009).

[12] E. Ding, E. Shlizerman, and J. N. Kutz, "Generalized master equation for high-energy passive mode-locking: the sinusoidal Ginzburg-Landau equation," IEEE J. Quant. Electron. **47**, 705-714 (2011).

[13] F. Li, P. K. A. Wai, and J. N. Kutz, "Geometrical description of the onset of multi-pulsing in mode-locked laser cavities," J. Opt. Soc. Am. B **27**, 2068-2077 (2010).

[14] R. Herda, O. G. Okhotnikov, E. U. Rafailov, W. Sibbett, P. Crittenden, and A. Starodumov, "Semiconductor quantum-dot saturable absorber mode-locked fiber laser," IEEE Photon. Technol. Lett. **18**, 157-159 (2006).

[15] S. Y. Set, H. Yaguchi, Y. Tanaka, and M. Jablonski, "Laser mode locking using a saturable absorber incorporating carbon nanotubes," J. Lightwave Technol. **22**, 51-56 (2004).

[16] S. Yamashita, Y. Inoue, S. Maruyama, Y. Murakami, H. Yaguchi, M. Jablonski, and S. Y. Set, "Saturable absorbers incorporating carbon nanotubes directly synthesized onto substrates and fibersand their application to mode-locked fiber lasers," Opt. Lett. **29**, 1581-1583 (2004).

[17] Z. Sun, T. Hasan, F. Torrisi, D. Popa, G. Privitera, F. Wang, F. Bonaccorso, D. M. Basko, and A. C. Ferrari, "Graphene mode-locked ultrafast laser," ACS Nano **4**, 803-810 (2010).

[18] H. Zhang, "Large energy soliton erbium-doped fiber laser with a graphene-polymer composite mode locker," App. Phys. Lett. **95**, 141103 (2009).

[19] H. Zhang, D. Y. Tang, L. M. Zhao, Q. L. Bao, and K. P. Loh, "Large energy mode locking of an erbium-doped fiber laser with atomic layer graphene," Opt. Express **17**, 17630-17635 (2009).

[20] F. Li, E. Ding, J. N. Kutz, and P. K. A. Wai, "Dual transmission filters for enhanced energy in mode-locked fiber lasers," Opt. Express **19**, 23408-23419 (2011).

[21] P. Grelu, W. Chang, A. Ankiewicz, J. M. Soto-Crespo, and N. Akhmediev, "Dissipative soliton resonance as a guideline for high-energy pulse laser oscillators," J. Opt. Soc. Am. B **27,** 2336-2341 (2010).

[22] E. Ding, P. Grelu, and J. N. Kutz, "Dissipative soliton resonance in a passively mode-locked fiber laser," Opt. Lett. **36**, 1146-1148 (2011).

[23] X. Shen, W. Li, M. Yan, and H. Zeng, "Electronic control of nonlinear-polarization-rotation mode locking in Yb-doped fiber lasers," Opt. Lett. **37**, 3426-3428 (2012).

[24] E. Ding and J. N. Kutz, "Operating regimes and performance optimization in mode-locked fiber lasers," Optics and Spectroscopy **111**, 166-177 (2011).

[25] C. R. Menyuk, "Pulse propagation in an elliptically birefringent Kerr media," IEEE J. Quant. Electron. **25**, 2674-2682 (1989).

[26] C. R. Menyuk, "Nonlinear pulse propagation in birefringent optical fibers," IEEE J. Quant. Electron. **23**, 174-176 (1987).

[27] K. B. Ariyur and M. Krstic . Real-Time Optimization by Extremum- Seeking Control. Wiley, Hoboken, New Jersey (2003).

[28] S. Backus, C. G. Durfee, M. M. Murnane, and H. C. Kapteyn. High power ultrafast lasers. Review of Scientific Instruments, 69(3):1207 1223 (1998).

[29] P. Binetti, K. B. Ariyur, M. Krstic , and F. Bernelli. Formation flight optimization using extremum seeking feedback. Journal of Guidance, Control, and Dynamics, 26(1):132142 (2003).

[30] A. I. Bratcu, I. Munteanu, S. Bacha, and B. Raison. Maximum power point tracking of grid-connected photovoltaic arrays by using extremum seeking control. CEAI, 10(4):312 (2008).

[31] S. L. Brunton and C. W. Rowley. Maximum power point tracking for photovoltaic optimization using ripple-based extremum seeking control. IEEE Transactions on Power Electronics, 25(10):25312540 (2010).

[32] J. Y. Choi, M Krstic , K. B. Ariyur, and J. S. Lee. Extremum seeking control for discrete-time systems. IEEE Transactions on Automatic Control, 47(2):318323 (FEB 2002).

[33] W. Denk, J. H. Strickler, and W. W. Webb. Two-photon laser scanning fluorescence microscopy. Science, 248(4951):7376 (1990).

[34] E. Ding and J. N. Kutz. Operating regimes, split-step modeling, and the Haus master mode-locking model. Journal of the Optical Society of America B, 26(12):22902300 (2009).

[35] E.Ding, W.H.Renninger, F.W.Wise, P.Grelu, E.Shlizerman and J.N. Kutz. High-energy passive mode-locking of fiber lasers. International Journal of Optics, 2012:117 (2012).

[36] T. Ditmire, J. Zweiback, V. P. Yanovsky, T. E. Cowan, G. Hays, and K. B. Wharton. Nuclear fusion from explosions of femtosecond laser-heated deuterium clusters. Nature, 398:489492 (1999).

[37] A. P. Joglekar, H. Liu, G. J. Spooner, E. Meyho fer, G. Mourou, and A. J. Hunt. A study of the deterministic character of optical damage by femtosecond laser pulses and applications to nanomachining. Applied Physics B, 77:2530 (2003).

[38] R. C. Jones. A new calculus for the treatment of optical systems. I. description and discussion of the calculus. Journal of the Optical Society of America, 31(7):488493 (1941).

[39] T. Juhasz. Corneal refractive surgery with femtosecond lasers. IEEE Journal of Selected Topics in Quantum Electronics, 5(4):902910 (1999).

[40] J. C. Kieffer, A. Krol, Z. Jiang, C. C. Chamberlain, E. Scalzetti, and Z. Ichalalene. Future of laser-based X-ray sources for medical imaging. Applied Physics B, 74:S75S81 (2002).

[41] A. D. Kim, J. N. Kutz, and D. J. Muraki. Pulse-train uniformity in optical fiber lasers passively mode-locked by nonlinear polarization rotation. IEEE Journal of Quantum Electronics, 36(4):465471 (2000).

[42] A. Komarov, H. Leblond, and F. Sanchez. Multistability and hysteresis phenomena in passively mode-locked fiber lasers. Physical Review A, 71:053809 (2005).

[43] M. Krstic and H. H. Wang. Stability of extremum seeking feedback for general nonlinear dynamic systems. Automatica, 36(4):595601 (April 2000).

[44] R. Leyva, C. Alonso, I. Queinnec, A. Cid-Pastor, D. Lagrange, and L. Martinez-Salamero. Mppt of photovoltaic systems using extremum- seeking control. IEEE Transactions On Aerospace and Electronic Systems, 42(1):249258 (January 2006).

[45] P. T. Mannion, J. Magee, E. Coyne, G. M. OConnor, and T. J. Glynn. The effect of damage accumulation behaviour on ablation thresholds and damage morphology in ultrafast laser micro-machining of common metals in air. Applied Surface Science, 233:275287 (2004).

[46] R. Maury, M. Keonig, L. Cattafesta, P. Jordan, and J. Delville. Extremum-seeking control of jet noise. Aeroacoustics, 11(3&4):459 474 (2012).

[47] C. R. Menyuk. Pulse propagation in an elliptically birefringent Kerr medium. IEEE Journal of Quantum Electronics, 25(12):26742682 (1989).

[48] I. Munteanu, A. I. Bratcu, and E. Ceanga. Wind turbulence used as searching signal for mppt in variable-speed wind energy conversion systems. Renewable Energy, 34(1):322327 (January 2009).

[49] J. Nilsson and D. N. Payne. High-power fiber lasers. Science, 332:921 922 (2011).

[50] Y. Ou, C. Xu, E. Schuster, T. C. Luce, J. R. Ferron, M. L. Walker, and D. A. Humphreys. Design and simulation of extremum-seeking open- loop optimal control of current profile in the DIII-D tokamak. Plasma Physics and Controlled Fusion, 50:115001111500124 (2008).

[51] M. Pastoor, L. Henning, B. R. Noack, R. King, and G. Tadmor. Feedback shear layer control for bluff body drag reduction. Journal of Fluid Mechanics, 608:161196 (2008).

[52] B. Ren, P. Frihauf, R. J. Rafac, and M. Krstic . Laser pulse shaping via extremum seeking. Control Engineering Practice, 20:674683 (2012).

[53] W. H. Renninger, A. Chong, and F. W. Wise. Dissipative solitons in normal-dispersion fiber lasers. Physical Review A, 77(2):0238141 0238144 (2008).

[54] W. H. Renninger, A. Chong, and F. W. Wise. Pulse shaping and evolution in normal-dispersion mode-locked fiber lasers. IEEE Journal of Selected Topics in Quantum Electronics, 18(1):389398 (2012).

[55] S. Toyran, Y. Liu, S. Singha, S. Shan, M. R. Cho, R. J. Gordon, and D. P. Edward. Femtosecond laser photodisruption of human trabecular meshwork: an in vitro study. Experimental Eye Research, 81:298305 (2005).

[56] A. Vogel, J. Noack, G. Hu ttman, and G. Paltauf. Mechanisms of femtosecond laser nanosurgery of cells and tissues. Applied Physics B, 81:10151047 (2005).

[57] A. Vogel and V. Venugopalan. Mechanisms of pulsed laser ablation of biological tissues. Chemical Reviews, 103(2):577644 (2003).

[58] H. H. Wang, M. Krstic , and G. Bastin. Optimizing bioreactors by extremum seeking. Adaptive Control and Signal Processing, 13(8):651 669 (1999).

[59] H. H. Wang, S. Yeung, and M. Krstic . Experimental application of extremum seeking on an axial-flow compressor. IEEE Transactions on Control Systems Technology, 8(2):300309 (2000).

[60] C. Xu and W. W. Webb. Measurement of two-photon excitation cross sections of molecular fluorophores with data from 690 to 1050 nm. Journal of the Optical Society of America B, 13(3):481491 (1996).

[61] A. H. Zewail. Femtochemistry. past, present, and future. Pure and Applied Chemistry, 72(12):22192231 (2000).

[62] C. Zhang and R. Ordonez. Numerical optimization-based extremum seeking control with application to ABS design. IEEE Transactions on Automatic Control, 52(3):454467 (2007).

[63] C. D. Poole and R. E. Wagner, "Phenomenological approach to polarization dispersion in long single-mode fibers," Electron. Lett. **22**, 1029–1030 (1986).

[64] P. K. A. Wai and C. Menyuk, "Polarization mode dispersion, decorrelation, and diffusion in optical fibers with randomly varying birefringence," J. Light. Tech. **14**, 148–157 (1996).

[65] J. P. Gordon and H. Kogelnik, "PMD fundamentals: polarization mode dispersion in optical fibers," PNAS **97**, 4541–4550 (2000).

[66] J. N. Kutz, "Mode-locked soliton lasers," SIAM Review **48**, 629–678 (2006).

[67] X. Fu and J. N. Kutz, "High-energy mode-locked fiber lasers using multiple transmission filters and a genetic algorithm," Opt. Express **21**, 6526–6537 (2013).

[68] S. L. Brunton, X. Fu, and J. N. Kutz, "Extremum-seeking control of a mode-locked laser," IEEE J. Quant. Electron. **49**, 852–861 (2013).

[69] X. Fu, S. L. Brunton, and J. N. Kutz, " Classification of birefringence in mode-locked fiber lasers using machine learning and sparse representation," Optics Express **22**, 8585-8597 (2014)

[70] D. Radnatarov, S. Khripunov, S. Kobtsev, A. Ivanenko, and S. Kukarin, "Automatic electronic-controlled mode locking self-start in fibre lasers with non-linear polarisation evolution," Opt. Express **21**, 20626–20631 (2013).

[71] S. Wiggins, *Introduction to Applied Nonlinear Dynamical Systems and Chaos*, Second Edition, (Springer 2003).

[72] J. Wright, A. Yang, A. Ganesh, S. Sastry, and Y. Ma, "Robust face recognition via sparse representation," IEEE Trans. Pattern Ana. Mach. Int. **31**, 210–227 (2009).

[73] D. Needell and J. A. Tropp, "CoSaMP: iterative signal recovery from incomplete and inaccurate samples," Comm. of the ACM **53**, 93–100 (2010).

[74] K. Pearson, "On lines and planes of closest fit to systems of points in space," Phil. Mag. **2**, 559-572 (1901).

[75] H. Hotelling, "Analysis of a complex of statistical variables into principal components," J. Educational Psychol. **23**, 498-520 (1933).

[76] K. Karhunen"Über lineare Methoden in der Wahrscheinlichkeitsrechnung," Ann. Acad. Sci. Fennicae. Ser. A. I. Math.-Phys. **37**, 1-79. (1947).

[77] M. Loéve, *Probability theory*, Vol. II, 4th ed. Graduate Texts in Mathematics 46 (Springer-Verlag,1978).

[78] L. Sirovich, "Turbulence and the dynamics of coherent structures. I - Coherent structures. II - Symmetries and transformations. III - Dynamics and scaling," Quart. Applied Math. **45**, 561-590 (1987).

[79] P. Holmes, J. L. Lumley, G. Berkooz, *Turbulence, Coherent Structures, Dynamical Systems and Symmetry* (Cambridge, 1998).

[80] J. N. Kutz, *Data-driven modeling and scientific computing* (Oxford, 2013).

[81] S. McCormick Ed. *Multigrid Methods (Frontiers in Applied Mathematics)*, (SIAM, Philadelphia, 1987)

[82] B. Engquist, O. Runborg, and Y.-H. Tsai Eds., *Numerical Analysis of Multiscale Computations: Proceedings of a Winter Workshop at the Banff International Research Station 2009*, Lecture Notes in Computational Science and Engineering, (Springer, New York, 2009).

[83] P.G. Martinsson, V. Rokhlin, and M. Tygert, "A randomized algorithm for the approximation of matrices". App. Comp. Harmonic Ana. **30**, 47-68 (2011).

[84] N. Halko, P. G. Martinsson, J. A. Tropp, "Finding Structure with Randomness: Probabilistic Algorithms for Constructing Approximate Matrix Decompositions," SIAM Rev. **53**, 217-288 (2011).

[85] N. Halko, P. G. Martinsson, Y. Shkolnisky and M. Tygert, "An algorithm for the principal component analysis of large data sets," SIAM J. Sci. Comput. **33**, 2580-2594 (2011).

[86] J. Xia, S. Chandrasekaran, M. Gu and X. S. Li, "Fast algorithms for hierarchically semiseparable matrices," Numer. Linear Algebra Appl. **17**, 953-976 (2010).

[87] M. Cross and P. Hohenberg, "Pattern Formation Outside of Equilibrium," Rev. Modern Phys. **65**, 851-1112 (1993).

[88] H. Schaeffer, S. Osher, R. Caflisch and C. Hauck, "Sparse Dynamics for Partial Differential Equations," arXiv:1212.4132 (2013).

[89] M. Williams, P. Schmid and J. N. Kutz, "Hybrid reduced-order integration with proper orthogonal decomposition and dynamic mode decomposition," SIAM Multiscale Model. Simul. **11**, 522-544 (2013).

[90] S. Chaturantabut and D. C. Sorensen "Nonlinear Model Reduction via Discrete Empirical Interpolation," SIAM J. Sci. Comput. **32**, 2737-2764 (2010).

[91] D. Amsallem, M. Zahr, C. Farhat, "Nonlinear Model Order Reduction Based on Local Reduced-Order Bases," Int. J. Numer. Meth. Engr. **92**, 891-916 (2012).

[92] R. Everson and L. Sirovich, "Karhunen-Loéve procedure for gappy data," J. Opt. Soc. Am. A **12**, 1657-1664 (1995).

[93] K. Wilcox, "Unsteady flow sensing and estimation via the happy proper orthogonal decomposition," Computers & Fluids **35**, 208-226 (2006).

[94] K. Carlberg, "Adaptive h-refinement for reduced-order models", arXiv:1404.0442v2.

[95] D. Dychelynck, F. Vincent and S. Cantournet, "Multidimensional *a priori* hyperreduction of mechanical models involving internal variables," Comput. Methods Appl. Mech. Engrg. **225-228**, 28-43 (2012).

[96] T. Kim and D. L. James, "Skipping steps in deformable simulation with online model reduction," Proceeding SIGGRAPH Asia '09 ACM SIGGRAPH Asia 2009 papers Article No. 123.

[97] I. G. Kevrekidis and G. Samaey "Equation-Free Multiscale Computation: Algorithms and Applications," Annu. Rev. Phys. Chem. **60**, 321-344 (2009).

[98] W. E, B. Engquist, X. Li, W. Ren, and E. Vanden-Eijnden, "The Heterogeneous Multiscale Method: A Review," Comm. Comp. Phys. **2**, 367-450 (2007).

[99] A. Zagaris, H. G. Kaper and T. J. Kaper, "Analysis of the Computational Singular Perturbation Reduction Method for Chemical Kinetics," J. Nonlinear Sci. **14**, 59-91 (2004).

[100] M. Marion and R. Temam, "Nonlinear Galerkin Methods," SIAM J. Numer. Anal. **26**, 1139-1157 (1989).

[101] C. Rowley

[102] N. L. Trefethen and D. Bau, *Numerical Linear Algebra* (SIAM 1997).

[103] C. Homescu, L. Petzold, R, Serban, "Error Estimation for Reduced-Order Models of Dynamical Systems," SIAM Rev. **49**, 277-299 (2007).

[104] J. N. Kutz and B. Sandstede, "Theory of passive harmonic mode-locking using waveguide arrays," Optics Express **16**, 636-650 (2008).

[105] M. Williams, E. Shlizerman, and J. N. Kutz, "The multi-pulsing transition in mode-locked lasers: a low-dimensional approach using waveguide arrays," J. Opt. Soc. Am. B **27**, 2471-2481 (2010).

[106] C. W. Rowley and J. E. Marsden, "Reconstruction Equations and the Karhunen-Loeve Expansion," Physica D **142**, 1-19 (2000).

[107] E. Ding, K. Lu and J. N. Kutz, "Stability analysis of cavity solitons governed by the cubic-quintic Ginzburg-Landau equation," J. Physics B **44**, 065401 (2011).

VITA

Xing Fu was born in Hangzhou, China. He received the B.S. degree in applied mathematics from the Sichuan University, Chengdu, China, in 2009, and a M.S. degree in applied mathematics from the University of Washington, Seattle, WA, in 2010. He then entered Ph.D. program in applied mathematics at the University of Washington, Seattle, WA.